Title: Summary report on UO2 thermal conductivity model refinement and assessment studies

Author(s): Liu, Xiang-Yang
Cooper, Michael William Donald
Mcclellan, Kenneth James
Lashley, Jason Charles
Byler, Darrin David
Bell, B.D.C.
Grimes, R.W.
Stanek, Christopher Richard
Andersson, Anders David Ragnar

Intended for: Report

Issued: 2017-02-03 (rev.1)

Summary report on UO_2 thermal conductivity model refinement and assessment studies

X.-Y. Liu[a], M. W. D. Cooper[a], K.J. McClellan[a], J.C. Lashley[b], D.D. Byler[a], B.D.C. Bell[c], R.W. Grimes[c], C. R. Stanek[a], D. A. Andersson[a]

[a]*Materials Science and Technology Division, Los Alamos National Laboratory P.O. Box 1663, Los Alamos, NM 87545, USA*
[b]*Sigma Division, Los Alamos National Laboratory, P.O. Box 1663, Los Alamos, NM 87545, USA*
[c]*Department of Materials, Imperial College London, London, SW4 7AZ, UK*

Abstract

Uranium dioxide (UO_2) is the most commonly used fuel in light water nuclear reactors and thermal conductivity controls the removal of heat produced by fission, therefore, governing fuel temperature during normal and accident conditions. The use of fuel performance codes by the industry to predict operational behavior is widespread. A primary source of uncertainty in these codes is thermal conductivity, and optimized fuel utilization may be possible if existing empirical models were replaced with models that incorporate explicit thermal conductivity degradation mechanisms during fuel burn-up. This approach is able to represent the degradation of thermal conductivity due to each individual defect type, rather than the overall burn-up measure typically used which is not an accurate representation of the chemical or microstructure state of the fuel that actually governs thermal conductivity and other properties. To generate a mechanistic thermal conductivity model, molecular dynamics (MD) simulations of UO_2 thermal conductivity including representative uranium and oxygen defects and fission products are carried out. These calculations employ a standard Buckingham type interatomic potential and a potential that combines the many-body embedded atom method potential with Morse-Buckingham pair potentials. Potential parameters for UO_{2+x} and ZrO_2 are developed for the latter potential. Physical insights from the resonant phonon-spin scattering mechanism due to spins on the magnetic uranium ions have been introduced into the treatment of the MD results, with the corresponding relaxation time derived from existing experimental data. High defect scattering is predicted for Xe atoms compared to that of La and Zr ions. Uranium defects reduce the thermal conductivity more than oxygen defects. For each defect and fission product, scattering parameters are derived for application in both a Callaway model and the corresponding high-temperature model typically used in fuel performance codes. The model is validated by comparison to low-temperature experimental measurements on single crystal hyper-stoichiometric UO_{2+x} samples and high-temperature literature data. Ongoing works include investigation of the effect of phase separation to $UO_2+U_4O_9$ on the low temperature thermal conductivity of UO_{2+x}, and modeling of thermal conductivity using the Green-Kubo method. Ultimately, this work will enable more accurate fuel performance simulations as well as extension to new fuel types and operating conditions, all of which improve the fuel economics of nuclear energy and maintain high fuel reliability and safety.

1. Introduction

Light water reactors (LWRs) generate heat from fission events and uranium dioxide (UO_2) is the most frequently used fuel. The thermal conductivity of UO_2 is a fundamentally important

property that governs nuclear reactor performance and safety. As the underlying property that controls temperature distribution, it affects thermal expansion, fission gas release and mechanical properties amongst other processes. It is favorable that high fuel pellet thermal conductivity be maintained during reactor operation so that efficient conversion of heat to electricity can be realized. It is also desirable that the fuel thermal conductivity be predictable. However, there are a number of processes that are known to degrade the thermal conductivity, such as radiation damage, compositional changes, point defects and microstructural features. Fuel performance codes [1–3] use thermal conductivity models [4], which empirically account for these complex phenomena, together with a number of other material models to investigate the behavior of fuel under a variety of conditions and evaluate margin to failure. Because almost all material properties are a function of temperature, e.g. fission gas release, the fuel thermal conductivity is the most important parameter from a model sensitivity perspective [5]. It is also one of the parameters with the highest uncertainty. Traditionally, empirical thermal conductivity models are derived from experiments and express the thermal conductivity as function of burn-up for a specific fuel type and operating conditions [6]. However, this is far from a solved problem, such that, the importance and challenges of improving UO_2 thermal conductivity models are emphasized by the continuing efforts by the nuclear industry to accomplish this goal [7, 8]. It is important, therefore, to develop more mechanistic thermal conductivity models that can account for the separate contributions of radiation damage and fission product concentrations [4]. This will allow conservative assumptions within fuel performance codes to be relaxed and enable more accurate predictions for high burn-up fuel reactor concepts and unusual accident conditions.

The importance of the thermal conductivity of nuclear fuel has motivated a wide range of experimental and modeling studies. Primarily, the thermal conductivity as a function of burn-up has been quantified by reviewing a large number of experimental studies [9–13]. As explained above, in order to evaluate fuel performance beyond conventional reactor conditions and burn-up limits one must have a detailed understanding of the underlying mechanisms for thermal conductivity reduction. Atomistic simulations can make important contributions to the deconvolution of the different processes that contribute to thermal conductivity degradation [4]. Previous studies of thermal conductivity utilizing atomistic simulations include thermal transport in bulk UO_2 [14–19], non-stoichiometric $UO_{2\pm x}$ [20–22], intrinsic defects [15, 22], grain-boundary effect [23], dislocations [24] and pores or bubbles [25]. Additionally, these effects have also been studied in mixed oxide fuels [26–28]. Of particular relevance to this study, the recent work of Tonks *et al.* [4] has predicted that the reduction of UO_2 thermal conductivity is significant even for low concentrations of Xe dispersed in the lattice. However, it was predicted that Xe accommodated at inter- or intra-granular bubbles has a much smaller effect, as there are fewer phonon scattering centers. Further work must be carried out to examine the distribution and scattering strength of various other fission products. In this paper, we expand upon the work of Tonks *et al.* [4] by using MD simulations to systematically investigate the reduction of thermal transport in UO_2 due to uranium and oxygen defects, fission products (Xe, La and Zr) and the transmutation product (Pu).

Magnetism has an important role in UO_2 thermal conductivity and should thus be included in the MD predictions. Scattering between phonons and spins on uranium ions occurs by phonon excitation of the magnetic ions, with the excited spin states at energy levels that are in the same range as the occupied phonons [29]. Phonon scattering by spins in UO_2 has been investigated experimentally [17, 30]. It demonstrates that, particularly at lower temperatures (≤ 300 K), UO_2 thermal conductivity is limited by spin-phonon scattering enabled by dynamic splitting of the cubic ground state of the uranium ions. This is based on the finding that above the Néel temperature T_N of 30.8 K, the paramagnetic phase of UO_2 exhibits dynamic Jahn-Teller

2

distortions in $\langle 100 \rangle$ lattice directions that split the ground state into three singlets with dispersive peaks of magnetic character between 3 and 10 meV, as identified from inelastic neutron scattering experiments [31, 32]. Without these splits, the excited states would be too high for interaction with phonons. Although attempts are being made to develop magnetic MD methods [33], spin dynamics cannot currently be captured. A description of parameters for magnetic scattering was derived in Ref. [17] by fitting a Callaway model to experimental data. Here the magnetic scattering contribution is combined with results from classical MD on perfect UO_2 to demonstrate the extent to which spin scattering accounts for the discrepancy between experiment and MD. The defect scattering term can then be determined by MD (without spin-phonon scattering) for the UO_2 lattice containing uranium and oxygen defects and the fission products Zr, La and Xe. The Callaway model parameters for these defective structures are combined with the experimental spin scattering contribution to give accurate predictions of the degradation of UO_2 thermal conductivity. These results are presented in a simple analytical form that can be implemented in fuel performance codes. Two sets of empirical potentials are used in this study, the pairwise potential developed by Busker *et al.* [34] and a many-body model developed by Cooper, Rushton and Grimes (CRG) [35].

The structure of this paper is as follows: First, a description of the methods employed in this work is presented. Second, the potential fitting results for Zr^{4+} and U^{5+} interactions, which are compatible with the CRG potential, are described. Third, the MD results and the Callaway model, adjusted by fitting to MD data for the thermal conductivity of UO_2 with uranium and oxygen defects and fission products, are analyzed. By fitting a simple analytical expression to the spin adjusted data, a host of defect scattering parameters are developed for implementation in fuel performance codes. Then, our modeling results are validated against low- and high-temperature experimental results for the thermal conductivity of UO_{2+x}. Last, ongoing works are briefly reported. These include investigation of the effect of phase separation to $UO_2 + U_4O_9$ on the low temperature thermal conductivity of UO_{2+x}, and modeling of thermal conductivity using an alternative MD method to compute the thermal conductivity, namely the Green-Kubo method.

2. Methods

2.1. Non-equilibrium MD simulations

In non-metallic solids, phonons dominate thermal transport. This provides the basis of the MD methodology for predicting the thermal conductivity of these materials. Here, we have employed the non-equilibrium MD method, which is often referred to as the "direct method" [36–38], where a heat current (J) is applied to the system and the thermal conductivity κ is computed from the time-averaged temperature gradient using Fourier's law,

$$\kappa = -\frac{J}{\partial T / \partial z} \tag{1}$$

A periodic supercell containing $n_x \times n_y \times n_z$ unit cells of fluorite UO_2 is constructed, where heat flow is in the z direction and $n_x = n_y < n_z$. For all MD simulations using the Busker potential $n_x = n_y = 3$, while for those that employ the CRG potential $n_x = n_y = 4$. The choices for n_x and n_y are based on the cut off distances used in the interatomic potentials. Regardless, the dependence of the computed thermal conductivity on cross sectional area has been shown to be weak [39].

1 nm thick hot and cold slabs are defined at $z = 0$ and $z = \frac{L_z}{2}$ from which heat is removed or added during the simulations, where L_z is the supercell length in the z direction. Although

other heat control mechanisms exist [37, 38], in this work the method of Jund and Jullien [36] has been employed, whereby a fixed amount of energy (ΔE) is added or subtracted from the hot and cold region by velocity rescaling every time step while preserving the total momentum of the atoms in the region. The original Jund and Jullien algorithm was derived for a single species system, nonetheless we found that it applies to systems with multiple species as well. Detailed benchmarking of the heat flux used in the non-equilibrium MD simulation of UO_2 has been carried out for different simulation conditions, such as temperature and supercell length. The heat flux used in the simulations is 1.1 - 3.7 $\times$ 10^{-4} eVnm^{-2} per time step. The temperature difference between hot and cold parts of the supercell is in the range of 40 - 360 K. The MD simulations were carried out using the LAMMPS code [40].

The system is initially equilibrated for 100 ps in the NVE ensemble at the desired temperature, with the volume of thermally expanded UO_2 lattice. Subsequently, non-equilibrium MD runs were performed under fixed heat flux for 10-26 ns, thus ensuring that steady state is reached in the first 4 ns. The temperature profile is averaged for the remaining time. $\partial T / \partial z$ is determined by taking the average of the gradients in the ranges $w < z < (\frac{L_z}{2} - w)$, and $(\frac{L_z}{2} + w) < z < (L_z - w)$, where $w = 0.13 L_z$ in line with earlier studies [41].

A key component of phonon scattering in MD simulations arises due to the hot and cold regions. Therefore, as L_z is increased the phonon mean free path associated with the separation of the hot and cold regions is also increased. There is a near-linear relationship [17] between the inverse of thermal conductivity and the inverse of L_z that can be extrapolated to determine the bulk thermal conductivity ($L_z^{-1} \rightarrow 0$). Here L_z is varied from 19 nm to 76 nm to enable extrapolation. For the remainder of the paper, κ is used for the extrapolated value of thermal conductivity from MD simulations.

In ionic materials, charged defects are common and a full treatment of their effect on thermal conductivity requires proper consideration of the corresponding charge compensating defects. In this work we consider three different cases of charge compensation:

1. Introduction of real charge compensating defects into the same simulation cell (for example, V_O, U^{5+} or U^{3+}). These defects create phonon scattering centers and reduce thermal conductivity. Whether they are introduced at random points in the cell or bound to the defect of interest, will affect the degradation in thermal conductivity.
2. Charge compensation by a uniform background charge (jellium). The uniform nature of the charge compensation means that it does not scatter phonons and the degradation in thermal conductivity is just due to the defect of interest.
3. A final consideration is to combine individual scattering strengths from (2) in proportions that represent charge neutral concentrations of defects. Due to the passive role of the uniform background charge in (2), this represents scattering strengths for defects in the dilute limit. One would expect similar results for (1) in the limit of weakly interacting randomly distributed defects.

These different approaches are applicable for different circumstances, as will be discussed throughout the manuscript.

2.2. Interatomic potentials

The short range interatomic potentials used in the MD studies have been previously developed by Busker *et al.* [34] and by Cooper *et al.* [35]. The Busker potential is implemented using the pairwise Buckingham potential form, while the CRG potential utilizes a combined Buckingham-Morse [42, 43] and embedded atom method (EAM) [44] potential approach.

The advantage of the Busker potential is the availability of a large parameter set with the ability to describe many fission products in UO_2. The Busker parameters used here have been

reported previously for U^{4+}-O^{2-}, O^{2-}-O^{2-}, Xe^{0}-U^{4+}, Xe^{0}-O^{2-}, La^{3+}-O^{2-} and Zr^{4+}-O^{2-} interactions [34, 45–47]. For U^{3+} and U^{5+} charge compensation of defects in UO_2, the U^{3+}-O^{2-} and U^{5+}-O^{2-} interactions reported in the literature [48, 49] are used.

Alternatively, the CRG potential provides a much better description of many thermophysical properties of UO_2, including the thermal expansion, specific heat and the elastic constants, than the Busker potential. Although the U^{4+}-U^{4+}, U^{4+}-O^{2-}, Pu^{4+}-O^{2-}, O^{2-}-O^{2-} and La^{3+}-O^{2-} interactions have been reported in the literature [35, 50, 51], the same number of fission product interactions as for the Busker potential does not exist. Therefore, it was necessary to develop a new parameter set for the U^{5+} and Zr^{4+} species (see Section 3). Interactions for Xe are not developed here as extensive density functional theory (DFT) calculations, which are beyond the scope of this work, would be required.

For computational efficiency, the Wolf summation method [52] is used throughout to compute the long-range Coulombic interactions. Formal and partial charges are employed for the Busker and the CRG potentials, respectively.

2.3. The Callaway model fitting procedure

According to the Callaway model [53], which assumes a Debye phonon spectrum, the thermal conductivity can be expressed in terms of the speed of sound, v, the phonon relaxation time, τ_p, the phonon frequency, ω, and the temperature, T:

$$\kappa = \frac{k_B}{2\pi^2 v} \left(\frac{k_B T}{\hbar} \right) \int_0^{\Theta_D/T} \frac{\tau_p x^4 e^x}{(e^x - 1)^2} dx \tag{2}$$
$$x = \hbar\omega/k_B T$$

where $\hbar$, Θ_D and k_B represent the reduced Plank constant, the Debye temperature and the Boltzmann constant respectively. The mean sound velocity v is taken to be 3171 m/s [17], and the Debye temperature Θ_D is 395 K [54].

The relaxation time is governed by various scattering processes that act to limit thermal conductivity. Typically included are point defect scattering (D), boundary scattering (B) and Umklapp processes (U), although in UO_2 it is also necessary to include spin scattering [29] (S) as an extension to the standard Callaway Model [17]. The inverse relaxation times can be combined according to the Matthiessen's relaxation rule such that $\tau_p^{-1} = \tau_D^{-1} + \tau_B^{-1} + \tau_U^{-1} + \tau_S^{-1}$, whereby the separate contributions are defined as:

$$\tau_D^{-1} = Dx^4 T^4 = D \left(\frac{\hbar\omega}{k_B} \right)^4 \tag{3}$$

$$\tau_B^{-1} = B \tag{4}$$

$$\tau_U^{-1} = UT^3 x^2 e^{-\Theta_D/bT} = UT \left(\frac{\hbar\omega}{k_B} \right)^2 e^{-\Theta_D/bT} \tag{5}$$

$$\tau_S^{-1} = \sum_i \frac{C_i \omega^4}{(\omega^2 - \omega_{S,i}^2)^2} F_i(T) \tag{6}$$

The spin scattering expression for τ_S^{-1} contains the resonance frequency, $\omega_{S,i}$, the phonon-spin coupling constant, C_i, and $F_i(T)$ which contains information about the two-level system ($i = 1, 2$), where $F_i(T) = (1 - e^{-\hbar\omega_{S,i}/k_B T})/(1 + e^{-\hbar\omega_{S,i}/k_B T})$. Fitting of D, B, U, b, C_1, C_2, $\hbar\omega_{S,1}$ and $\hbar\omega_{S,2}$ to experimental data has previously been conducted by Gofryk et al. [17] and is reported in Table 1 for the $\langle 110 \rangle$ direction.

Table 1: Callaway model parameters from Gofryk *et al.* [17] that were fitted to experimental thermal conductivity in the $\langle 110 \rangle$ directions.

Defect, boundary and Umklapp terms			
D (K^{-4}s^{-1})	B (s^{-1})	U (K^{-3}s^{-1})	b
267.8	2.422×10^8	31510	2.166
Spin scattering terms			
C_1 (s^{-1})	C_2 (s^{-1})	$\hbar\omega_{S,1}$ (eV)	$\hbar\omega_{S,2}$ (eV)
1.120×10^{12}	2.669×10^{12}	0.003525	0.003429

The defect (D), boundary (B), Umklapp (U, b) parameters make up the classical phonon scattering components of thermal conductivity, which can be fitted to the results of MD. However spin scattering, which is not captured by MD simulations, must subsequently be introduced through the Callaway model using the experimentally determined parameters reported in Table 1. The approach used in this work can be summarized as, i) initially D (or D_{pure} in equation 7), B, U and b are all fitted to the MD results for pure UO$_2$ (with spin scattering excluded from the model); then ii) the experimentally determined C_1, C_2, $\omega_{S,1}$ and $\omega_{S,2}$ from Table 1 are reintroduced. This provides a version of the Callaway model for pure UO$_2$ that combines classical contributions determined from MD with the experimental magnetic effects and accounts for significant discrepancies between modeling and experiment. Subsequently, it is possible to refit only the defect scattering term (D) to MD data for the defective UO$_2$ lattice (B, U and b are maintained from the pure UO$_2$ fitting). The linear relationship between D and the defect concentration, x, shown in equation 7 is enforced such that a single D' is required for each defect species.

$$D = D_{pure} + D'x \tag{7}$$

where the defect concentration, x, is defined as the number of defects divided by the total number of atoms in the otherwise perfect UO$_2$ supercell. Note that this is different from "available site" fraction (C_s). For example, in the V_U case, x equals one third of C_s and for V_O, it equals two thirds of C_s.

By reintroducing the experimental spin scattering parameters an accurate description of the degradation of thermal conductivity due to defect accumulation is obtained. Any coupling between spin and defects is ignored, as defect concentrations investigated here are assumed to be low enough not to influence UO$_2$ magnetism.

2.4. Simple analytical expression for defect scattering

Many fuel performance codes take expressions for defect scattering that are simpler than the Callaway model. These expressions are based on a proportional relationship between thermal conductivity and the effective phonon mean free path, $\kappa \propto l_{eff}$, that is valid at high temperature. Furthermore, by assuming a constant phonon group velocity and using Matthiessen's phonon relaxation rule, one can derive the following expression for thermal conductivity:

$$\kappa = \frac{1}{A + BT + Cx} \tag{8}$$

where T is the temperature and x is the defect concentration, as defined previously. Phonon scattering processes are split into defect scattering (C), Umklapp scattering (B) and miscellaneous scattering (A). For fitting these parameters, MD data above 500 K that has been corrected for spin scattering through the Callaway model is used. A and B parameters are fitted to the pure UO$_2$ thermal conductivity as a function of temperature. Subsequently, A and B are fixed while C is adjusted for each defect species in a similar fashion to the D' Callaway parameter.

3. Fitting ZrO$_2$ EAM potential

3.1. Fitting procedure

Similar to previous centrosymmetric potentials, such as pair potentials [55], the EAM potential form (in [35] for the CRG potential) could not stabilize the monoclinic ZrO$_2$ crystal structure. Fitting was carried out to the tetragonal elastic constants from DFT and the tetragonal experimental lattice parameters [56–58].

- Elastic constants predicted by the potential from energy minimization in GULP [59] were fitted to the DFT elastic constants. DFT elastic constants were obtained by simulations using the CASTEP code with the PBE exchange-correlation functional [60], ultra-soft pseudo potentials, a consistent plane-wave cut-off energy of 550 eV and a Monkhorst-Pack [61] k-point grid of 4×4×4. The fully relaxed conventional unit cell was deformed along symmetry independent directions by 5 strain increments of 0.01. Each perturbation was relaxed again with tight convergence criteria (energy differential $< 10^{-6}$ eV), and the energy landscape was used to extract the stiffness constants using the tools developed by Walker and Wilson [62].

- The temperature dependence of the tetragonal ZrO$_2$ lattice constants predicted by the potential in MD simulations using LAMMPS [40] were fitted to the room temperature data of Bondars *et al.* [56] and high temperature XRD data from Aldebert and Traverse [57] and Teufer [58].

At each iteration of the fitting procedure the tetragonal ZrO$_2$ structure was equilibrated at 300 K and 1600 K for 20 ps with the lattice parameters averaged over the final 10 ps. Simultaneously, the 0 K elastic constants were determined using GULP [59]. By comparison to the experimental lattice parameters at the relevant temperature and the DFT elastic constants, the potential parameters were iteratively refined to improve the match.

To be consistent with the previous actinide oxide potential set, the O^{2-}-O^{2-} parameters were fixed at their previous values and the partial charges are proportional to their formal values such that $q_\alpha = Z_\alpha^{eff}|e|$, where $Z_{Zr}^{eff} = 2.2208$ and $Z_O^{eff} = $ -1.1104. This consistency enabled the degradation of UO$_2$ thermal conductivity due to Zr$_U$ substitutional defects to be investigated.

Additionally, the mixed cation U^{4+}-Zr^{4+} interactions were defined in similar terms to previous mixed cation parameters [63], such that $A_{U^{4+}Zr^{4+}} = 18600$ eV and $\rho_{Zr^{4+}Zr^{4+}}$ is scaled to cation radii [64]. Subsequently, $\rho_{U^{4+}Zr^{4+}}$ is determined from $\rho_{Zr^{4+}Zr^{4+}}$ and $\rho_{U^{4+}U^{4+}}$ by using

$$\rho_{\alpha\beta} = (\rho_{\alpha\alpha}.\rho_{\beta\beta})^{\frac{1}{2}} \qquad (9)$$

The final parameter set derived by the fitting process is summarized in Table 2.

3.2. Comparison with DFT

Tables 3 and 4 report the elastic constants and lattice parameters predicted by the new EAM potential. The DFT predictions used in the fitting are included for comparison. A reasonable agreement is achieved for all single crystal elastic constants with the exception of C$_{33}$ and C$_{13}$. However, this relates to the strain associated with the c lattice parameter, which, as can be seen in Table 4, is significantly overestimated by DFT compared to the experimental data used to fit the potential. It is important to note that there is no fitting to the DFT lattice parameters.

Comparison with a range of DFT data from the literature shows good agreement with the potential for all single crystal elastic constants. Furthermore, the lattice constants lie within the range of DFT values and the agreement with the experimental data is also good.

Table 2: Potential parameters for ZrO_2 using the same potential form as reported previously [35]. O-O parameters are also unchanged from the previous work.

	Pair parameters		
	Zr^{4+}-U^{4+}	Zr^{4+}-Zr^{4+}	Zr^{4+}-O^{2-}
$A_{\alpha\beta}$ (eV)	18600	18600	1147.471
$\rho_{\alpha\beta}$ (Å)	0.25172	0.23066	0.32235
$C_{\alpha\beta}$ (eVÅ^6)	0.0	0.0	0.0
$D_{\alpha\beta}$ (eV)	-	-	1.2269
$\gamma_{\alpha\beta}$ (Å^{-1})	-	-	1.4482
$r^0_{\alpha\beta}$ (Å)	-	-	1.998
	EAM parameters		
G_{Zr} (eVÅ$^{1.5}$)	1.597		
n_{Zr} (Å^5)	1188.786		

Although not used in the fitting procedure, the experimental values for the elastic constants of Ce-doped ZrO_2 by Kisi and Howard [65] are also included in Table 3. However, it is unclear to what extent Ce-doping alters the elastic constants.

Table 3: Elastic constants predicted by the potential alongside the DFT values used in fitting. Additional DFT data and experimental results for Ce-doped ZrO_2 are included for comparison.

	Fitting Data		Validation Data	
(GPa)	EAM Potential	DFT (present study)	DFT [66–69]	Exp. (Ce-doped) [65]
C_{11}	338	334.25	293 - 401	327
C_{33}	313	251	248 - 385	264
C_{44}	41.7	9.37	9.08 - 51.0	59
C_{66}	166	153	152 - 187	64
C_{12}	229	207	211 - 248	100
C_{13}	94.2	48.9	51.9 - 111	62

Table 4: Static lattice constants and comparison with DFT data.

			Validation Data	
(Å)	EAM Potential	DFT (present study)	DFT [66–69]	Exp. [70, 71]
a	3.60	3.62	3.27-3.61	3.59-3.60
c	5.19	5.28	5.14-5.28	5.18

3.3. Comparison with experimental thermal expansion

Figure 1 shows thermal expansion of the *a* and *b* lattice parameters as predicted using the new potential; there is a good agreement with the experimental values over a wide range of temperatures. Likewise, the agreement for the lattice parameter *c* is also good (see Figure 2).

The sudden change in behavior at ≈2000 K in Figures 1 and 2 seems to indicate a phase transition. If this is due to the high temperature fluorite phase of ZrO_2 (lattice parameter =

8

a_{cubic}) then the following relationship should be true:

$$a_{cubic} = c = \sqrt{a^2 + b^2} = a\sqrt{2}$$

$$\frac{a}{c} = \frac{\sqrt{2}}{2} = 0.7071 \tag{10}$$

It can be seen in Figure 3 that the tetragonal to fluorite phase change occurs at 2000 K. This is significantly different than the value of 2650 K shown in the phase diagram [72]. The previous potential of Schelling *et al.* [55] also exhibits a phase transition at 2000 K. Additionally, it should be noted that in Figure 3 the experimental results seem to indicate that the phase transition is beginning to occur below the temperature given in the phase diagram [72].
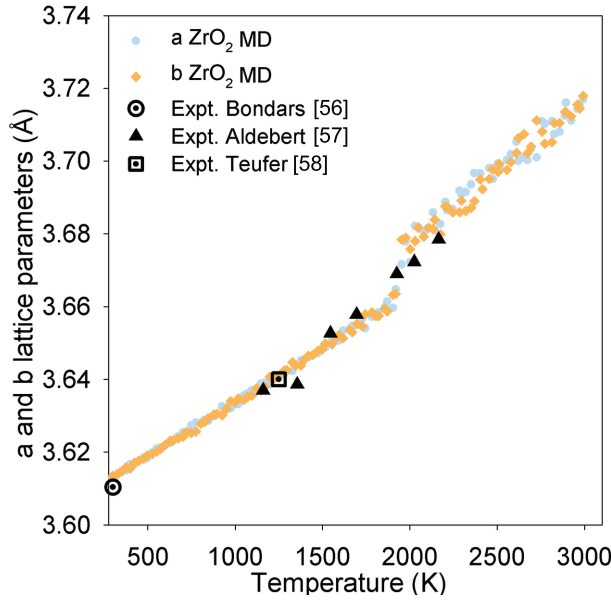
Figure 1: The variation of the a and b lattice parameters of tetragonal ZrO_2 as a function of temperature using the new potential with comparison to experimental data [56–58].

4. Fitting UO_{2+x} EAM potential

Under hyper-stoichiometric conditions (UO_{2+x}), U^{4+} becomes oxidized to U^{5+}. It is, therefore, necessary to derive suitable parameters for the description of U^{5+}-O^{2-}, U^{5+}-U^{4+} and U^{5+}-U^{5+} interactions. For the cation-cation interactions, the covalent Morse term was omitted, as was the dispersive interaction within the Buckingham term. The remaining A and ρ Buckingham parameters for the U^{5+}-U^{5+} interactions were determined in a similar fashion to previous cation terms [63]; $A_{U^{5+}U^{5+}}$ was fixed at 18600 eV and $\rho_{U^{5+}U^{5+}}$ was scaled to the U^{5+} ionic radius [64] giving 0.24287 Å. The mixed cation $\rho_{U^{5+}U^{4+}}$ parameter was determined using equation 9. The many-body EAM parameters for U^{5+} remain unchanged from the U^{4+} CRG case.

The U^{5+}-O^{2-} pair interactions were fitted to the DFT structure for U_4O_9 reported previously by Andersson *et al.* [73] by adjusting the relevant potential parameters in order to minimize the interatomic forces for that structure. The DFT structure calculated by Andersson *et al.* [73]
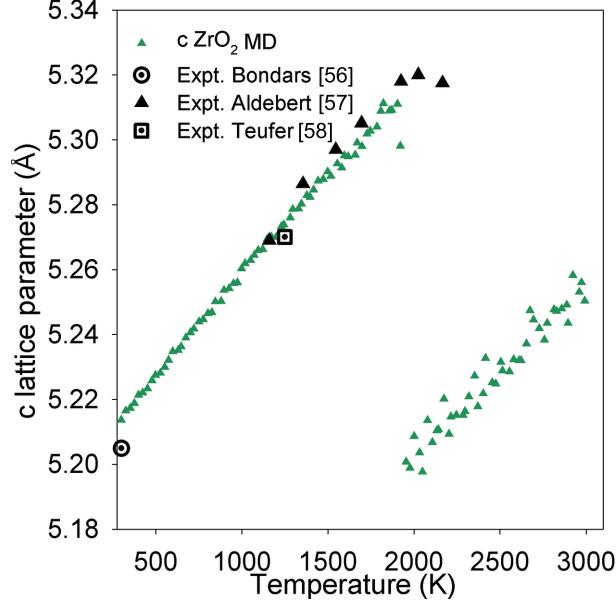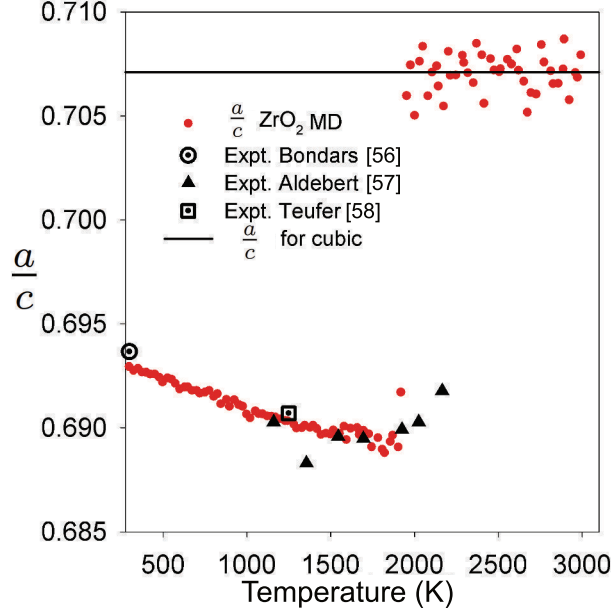
Figure 2: The variation of the c lattice parameter of tetragonal ZrO_2 as a function of temperature using the new potential with comparison to experimental data [56–58].

is shown in Figure 4a with U^{5+} ions highlighted in blue. External pressure on the supercell was omitted from fitting as disagreement between the DFT and empirical potential lattice parameter for UO_2 makes this unreliable. Therefore, fitting was simultaneously carried out to the experimental change in lattice parameter as a function of hyper-stoichiometry, x, [74, 75] by equilibrating $5\times5\times5$ $UO_{2.1}$ fluorite supercells at 300 K over 20 ps and determining the lattice parameter over the final 10 ps. This equilibration was carried out on five different supercell configurations where I_O anions and U^{5+} cations were randomly distributed throughout the lattice.

The final parameter set for U^{5+} derived by the fitting process is summarized in Table 5. As for ZrO_2 potential fitting, the O^{2-}-O^{2-} parameters are unchanged and $Z^{eff}_{U^{5+}} = 2.7760$.

Table 5: Potential parameters for U^{5+} using the same potential form reported previously [35]. U^{4+}-O^{2-}, U^{4+}-U^{4+} and O^{2-}-O^{2-} parameters are kept the same as for the previous actinide oxide potential set [35].

	Pair parameters		
	U^{5+}-U^{4+}	U^{5+}-U^{5+}	U^{5+}-O^{2-}
$A_{\alpha\beta}$ (eV)	18600	18600	1155.631
$\rho_{\alpha\beta}$ (Å)	0.25829	0.24287	0.34648
$C_{\alpha\beta}$ (eVÅ^6)	0.0	0.0	0.0
$D_{\alpha\beta}$ (eV)	-	-	1.9317
$\gamma_{\alpha\beta}$ (Å^{-1})	-	-	1.4881
$r^0_{\alpha\beta}$ (Å)	-	-	2.0709
EAM parameters			
$G_{U^{5+}}$ (eVÅ$^{1.5}$)	1.806		
$n_{U^{5+}}$ (Å^5)	3450.995		

10

Figure 3: The variation of $\frac{a}{c} = 0.7071$ for tetragonal ZrO_2 as a function of temperature using the new potential with comparison to experimental data [56–58]. When $\frac{a}{c} = 0.7071$ the tetragonal structure has changed to the fluorite structure (i.e. above 2000 K).

The atomic forces were not completely minimized during fitting and the average atomic force is 0.147 eVÅ^{-1} when using the parameter set in Table 5 in conjunction with the DFT structure [73] (see Figure 4a). This approach represents a reasonable agreement with the fitting data. However, the maximum force on a single atom was 2.78 eVÅ^{-1} indicating that some atoms will move noticeably during relaxation. The fully relaxed structure predicted by the new potential is shown in Figure 4b, thus confirming differences compared to the predicted DFT structure. However, this is not unexpected due to the far more complex interactions of a DFT calculation.

Figure 5 shows a favorable agreement with the change in experimental and DFT lattice parameters, a, as a function of hyper-stoichiometry, x, for UO_{2+x}. This is shown by the close agreement in the slope $\frac{da}{dx}$ and indicates that the new potential provides a good description of the U^{5+} defect volume.

5. Results

5.1. Pure UO_2

Figure 6 shows the results of fitting the Callaway model without spin scattering to the MD data for pure UO_2 (red lines) for a) the Busker potential and b) the CRG potential. The data for the Busker potential was calculated as a part of previous work [4], however, in this case MD data below 300 K was omitted due to inconsistencies between empirical potentials and the low temperature experimental specific heat [63, 80, 81]. The classical MD simulations cannot capture the very low temperature thermal conductivity where quantum effects dominate. Typically, a T^3 dependence of thermal conductivity would appear which is associated with the T^3 dependence of the specific heat. However, the MD results that have been fitted to the Callaway model do capture the T^3 dependence, as the correct low-temperature behavior is imposed by the form of
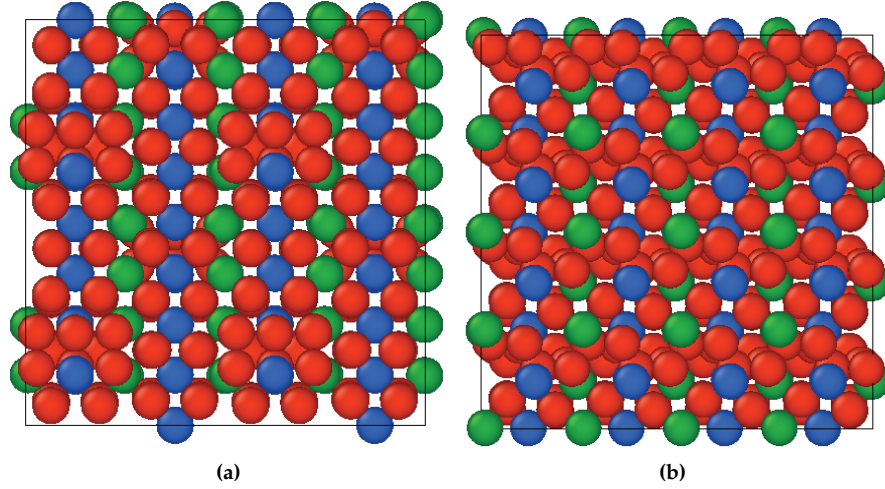
Figure 4: The U_4O_9 structure predicted by a) DFT [73] and b) the new potential (Table 5). U^{5+}, U^{4+} and O^{2-} ions are indicated by blue, green and red spheres, respectively.

the Callaway model. The fitted result at low temperature is inherently an extrapolation of the UO_2 properties at higher temperature.

A good agreement is obtained between the fitted Callaway model (parameters reported in Table 6) and the MD data. It can be seen that the thermal conductivity is predicted to be higher for the Busker potential than for the CRG potential, although both potentials predict a higher thermal conductivity than the experimental values, particularly at low temperatures where spin scattering is significant.

The D_{pure}, B, U and b parameters reported in Table 6 for the Busker and CRG potentials are combined with the C_1, C_2, $\hbar\omega_{S,1}$ and $\hbar\omega_{S,2}$ parameters in Table 1 in order to account for the experimental spin scattering. Figure 6 shows that the modeling results adjusted for spin scattering (blue lines) are greatly improved for the CRG and Busker potentials. Furthermore, Figure 6b) shows that spin scattering accounts for virtually all discrepancy between the CRG potential and experiment above 300 K. It should be noted that some factors remain, which may account for the differences below 300 K. For example, there could be defects in the experimental samples due to material processing or slight off-stoichiometry. Another potentially significant factor is that empirical potentials typically overestimate the specific heat capacity at low temperatures [63, 80, 81]. Finally, as suggested previously [17], the experimental boundary parameter B may be accounting for some degree of spin scattering. Thus, by adjusting B when fitting to the MD results the effect of spin scattering might be underestimated.

Despite the improvement achieved by including the experimental spin scattering components, the Busker potential remains higher than the experimental values. This is also true in the high temperature Umklapp dominated region [82] where magnetic effects are limited. It indicates that spin scattering is not sufficient to account for discrepancies between the Busker potential and experiment. This may be due to the dependence of the longitudinal and transverse phonon group velocities (v_L and v_T) on the elastic constants [55]: $v_L = \sqrt{C_{11}/\rho}$ and $v_L = \sqrt{C_{44}/\rho}$. Thus, the Busker potential over-predicts the phonon group velocity by over-predicting the C_{44} elastic constant (note that $C_{44} = C_{12}$ for the Busker potential since it contains only two-body potentials). Conversely, the CRG potential, which gives a much more accurate prediction of the single crystal elastic constants [35] is very close to the experimental thermal
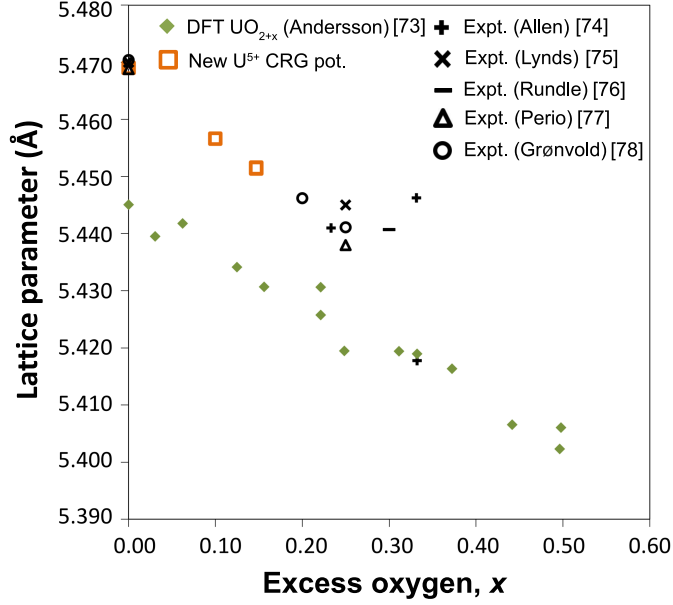
Figure 5: Lattice parameter of UO_{2+x} predicted by the new potential compared to available experimental [74–78] and DFT [73] data.

conductivity once it has been adjusted to include spin scattering. This indicates that the CRG potential provides a better description of thermal transport in the classical lattice.

Table 6: Non-magnetic Callaway model parameters for pure UO_2 shown for both the Busker potential and the CRG potential.

Busker potential			
D_{bulk} ($K^{-4}s^{-1}$)	B (s^{-1})	U ($K^{-3}s^{-1}$)	b
80.41	2.174×10^8	20540	2.554
CRG potential			
D_{bulk} ($K^{-4}s^{-1}$)	B (s^{-1})	U ($K^{-3}s^{-1}$)	b
154.9	4.222×10^7	40910	1.827

5.2. Fission products (Zr^{4+}, La^{3+} and Xe^0) and a transmutation product (Pu^{4+})

MD simulations of the thermal conductivity of UO_2 containing the fission products Zr, La, Xe and the transmutation product Pu are now reported. Zr and La atoms substitute for a single uranium cation, whereas Xe is accommodated in a Schottky vacancy site, V_{UO_2}, based on earlier DFT+U calculation results [83, 84]. The Schottky vacancy consists of one U vacancy and two O vacancies bound together. These are expected to be the energetically most favorable incorporation sites for the respective fission products. The substitution sites are randomly distributed using a pseudo random number generator. There is a charge imbalance of -1 when La^{3+} is introduced at a U^{4+} site, therefore, for every La^{3+} ion one U^{5+} ion is randomly substituted at a U^{4+} site to ensure full charge compensation. Charge compensation of La^{3+} by U^{5+} is expected in
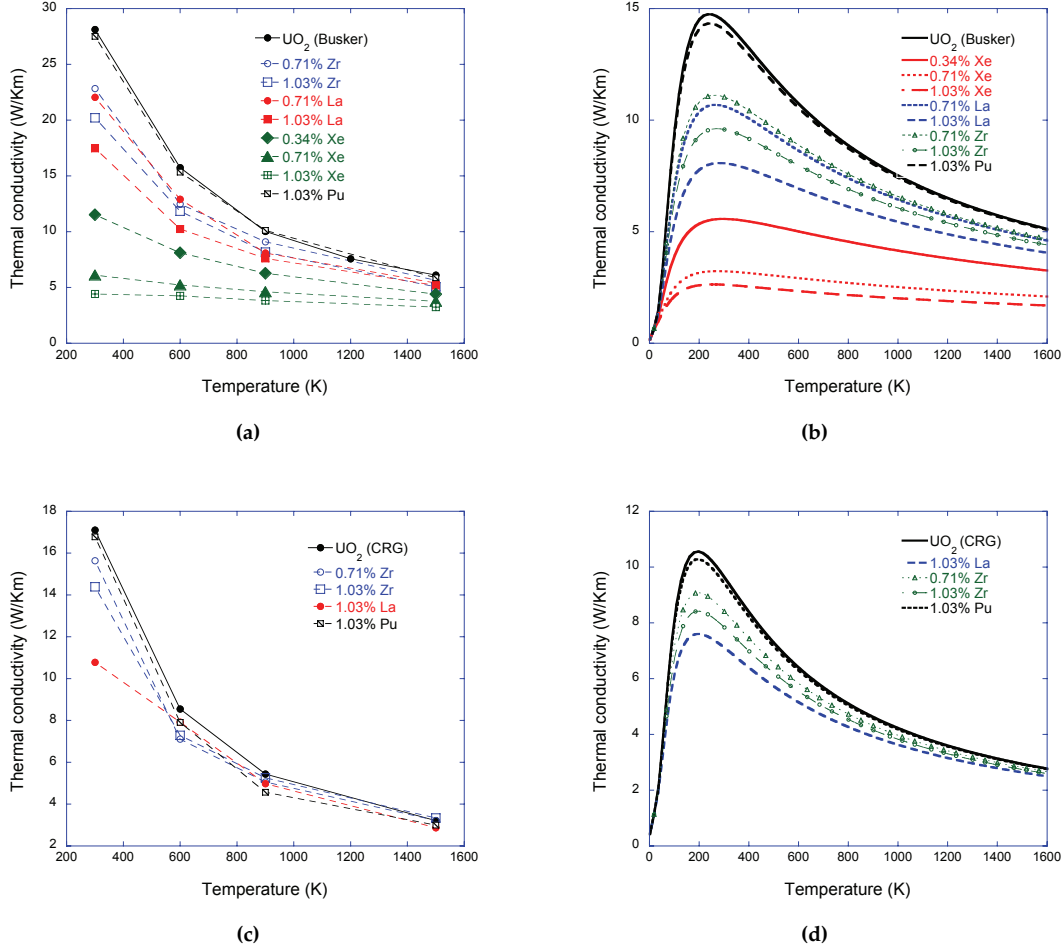
13
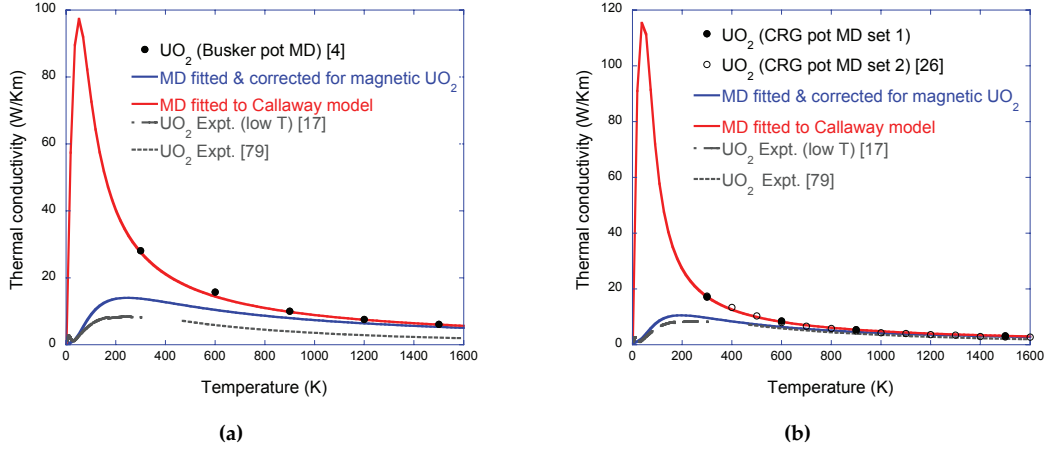
Figure 6: (a) MD simulation of the UO_2 thermal conductivity employing the Busker Buckingham potential, both with and without correction for spin-phonon scattering. The spin-phonon scattering correction was derived by fitting a Callaway model to the experimental data [17, 79] and then adding the spin-phonon relaxation time to the MD results. (b) Similar to (a) but employing the CRG potential.

UO_{2+x} and UO_2 [85], although some charge compensation in UO_2 is predicted to also occur by oxygen vacancies [86, 87] (as will be addressed in section 5.6). The U^{5+} cations are distributed independently of the La^{3+} positions, according to the expected high temperature behavior.

Figures 7a (Busker) and 7c (CRG) show the MD results for the thermal conductivity of UO_2 with atomic concentrations of La, Zr, Xe and Pu ranging from 0.34% to 1.03%, which is a relevant range of expected fission product concentrations. Note that results for Xe are not included for the CRG potential as a suitable parameter set does not yet exist. For both potentials a greater degradation of the UO_2 thermal conductivity is predicted for La^{3+} than for Zr^{4+} despite the greater mismatch in ionic radii [64] between U^{4+} (1.00 Å) and Zr^{4+} (0.72 Å) compared to the mismatch with La^{3+} (1.16 Å). This apparent discrepancy is due to the additional introduction of U^{5+} cations, which have their own scattering contribution, necessitated by the charge imbalance of La^{3+} accommodation at the U^{4+} site. Furthermore, the transmutation product Pu^{4+} exhibits an even smaller effect than Zr^{4+} due to its isovalent accommodation in UO_2 as well as a similar ionic radius (0.96 Å) to that of U^{4+}. It can be seen in Figure 7a that, compared to the other fission products, Xe severely reduces the thermal conductivity. For example, using the Busker potential at room temperature a concentration of just 0.34% Xe reduces the thermal conductivity from $28.1\,WK^{-1}m^{-1}$ to $11.5\,WK^{-1}m^{-1}$, whereas, Zr and La exhibit much weaker phonon scattering. For example, even with a comparatively high 1.03% concentration of La the room temperature value remains as high as $17.5\,WK^{-1}m^{-1}$.

For accurate prediction of the thermal conductivity of UO_2, including impact of fission product accumulation, it is important to adjust the MD results to include spin scattering. As for the pure UO_2 case, the Callaway model without spin scattering is fitted to the data reported in Figures 7a (Busker) and 7c (CRG). However, only the defect scattering parameter (D', see equation 7) is adjusted, while D_{pure}, B, U and b are fixed from the fitting to pure UO_2 MD data. Unlike previous work where all Callaway parameters were readjusted [4], by allowing only D' to vary consistent comparison can be made between different defect types and concentrations (see Section 5.4). By then reintroducing the experimental spin scattering parameters, the MD

14

Figure 7: (a) Thermal conductivity of UO$_2$ at different temperatures of 0.71 and 1.03 atomic percent Zr, 0.71 and 1.03 atomic percent La, 0.34, 0.71, and 1.03 atomic percent Xe and 1.03 atomic percent Pu. Thermal conductivity of UO$_2$ at different temperatures obtained using the Busker Buckingham potential is also plotted for comparison. (b) Thermal conductivities of UO$_2$ containing Xe, La, Zr and Pu, including correction for spin-phonon scattering. These results were obtained from the data in (a) by adding the spin-phonon scattering contribution derived from experimental data. (c) Thermal conductivity of UO$_2$ at different temperatures of 0.71 and 1.03 atomic percent Zr, and 1.03 atomic percent La and Pu employing the CRG potentials. Thermal conductivity of UO$_2$ at different temperatures obtained using the CRG potential is also plotted for comparison. (d) Thermal conductivity of UO$_2$ containing La and Zr including correction for spin-phonon scattering. These results were obtained from the data in (c).

15

results are adjusted accordingly and are reported as a function of temperature in Figures 7b and 7d for the Busker potential and the CRG potential, respectively. In all cases the reduction in thermal conductivity due to defects is less dramatic when spin scattering is included compared to the pure MD case. This difference is because spin scatting has already reduced the phonon relaxation time. Regardless, there is a very strong defect scattering strength associated with Xe. This may be in part due to the large Schottky defects that accommodate Xe. In the future, coupling of the diffusion of fission products [4, 88, 89] to thermal transport of such fission products will be considered. For example, the importance of Xe on thermal transport has been predicted by Tonks *et al.* [4] to depend greatly on how it is accommodated in the fuel, whereby, Xe in bubbles has a smaller effect compared to Xe dispersed throughout the UO_2 matrix. Similarly, the distribution of other fission products in metallic or oxide precipitates [90–92] may alter their effects on the thermal conductivity of nuclear fuel. Alternatively, high temperatures resulting from low thermal conductivity will enhance fission gas release [93] and, thus, reduce the concentration of fission gas atoms dispersed within the UO_2 lattice. This may account for some degree of thermal conductivity recovery and is just one example of how coupling our results with other phenomenological models can help fuel performance codes capture these complex and inter-related processes.

5.3. Oxygen and uranium defects

To account for radiation damage and non-stoichiometry, uranium and oxygen defects must also be studied. Here we considered oxygen interstitials (I_O), oxygen vacancies (V_O), uranium interstitials (I_U) and uranium vacancies (V_U). In all cases U^{5+} and U^{3+} species were introduced by random distribution in appropriate proportions to achieve full charge compensation (e.g. I_O+2U^{5+} or V_O+2U^{3+}). In both the stoichiometric and hyper-stoichiometric range where we are most interested, V_U is primarily charge compensated by holes instead of by anion defects. In the hypo-stoichiometric range, charge compensation is predicted to also occur by oxygen vacancies (as will be discussed in section 5.6). Note that due to the lack of a U^{3+} parameter set for the CRG potential V_O and I_U were only investigated using the Busker potential. The role of background charge compensated defects will be considered in section 5.6 as well. All isolated interstitial species are located at the 4b Wyckoff positions.

Firstly, we investigated the effect of oxygen defects on thermal conductivity. Figure 8a (Busker) shows the effect of I_O+2U^{5+} ($x > 0$) and V_O+2U^{3+} ($x < 0$) on the thermal conductivity of UO_{2+x} as a function of concentration for several temperatures. These non-spin adjusted results for the Busker potential show a similar thermal conductivity degradation regardless of whether $x < 0$ or $x > 0$. Secondly, the effect of uranium defects, V_U+4U^{5+} ($x > 0$) and I_U+4U^{3+} ($x < 0$), on thermal conductivity is investigated; the results are shown in Figure 8c. Again the degradation in thermal conductivity is predicted to be symmetrical about $x = 0$, however the effect of non-stoichiometry is more significant for uranium defects.

Figure 9a (CRG) shows the thermal conductivity of UO_{2+x} determined by including I_O or V_U in MD simulations. As for the Busker potential, the CRG potential predicts a greater degradation in thermal conductivity due to uranium defects than oxygen defects. Although the trends for the thermal conductivity degradation are similar between the two potentials, the absolute values for the CRG potential are lower, which is in line with the predictions made for pure UO_2 (see Figure 6).

By fitting the Callaway D' parameter to the data in Figures 8a, 8c and 9a and then introducing the experimentally determined spin scattering components, as was done for the fission products, a more accurate prediction of the thermal conductivity degradation due to defects is made. Figures 8b, 8d (Busker) and 9b (CRG) show that the results are reduced to levels close to experiments by the incorporation of spin scattering. Furthermore, the degradation remains
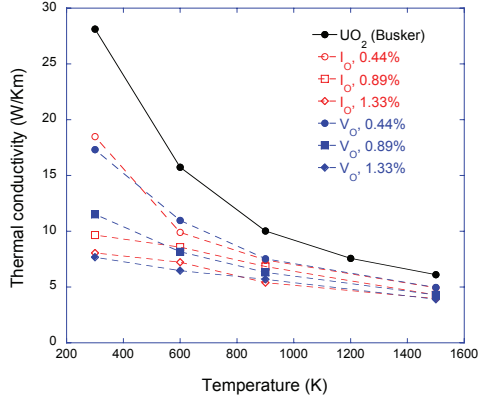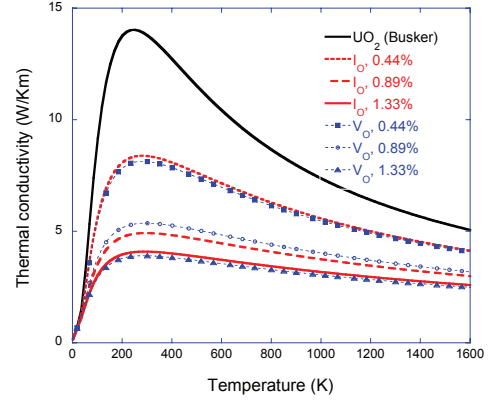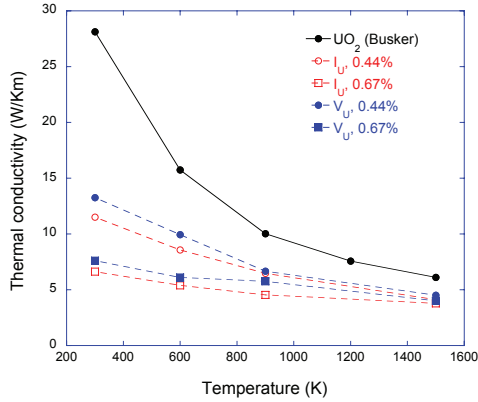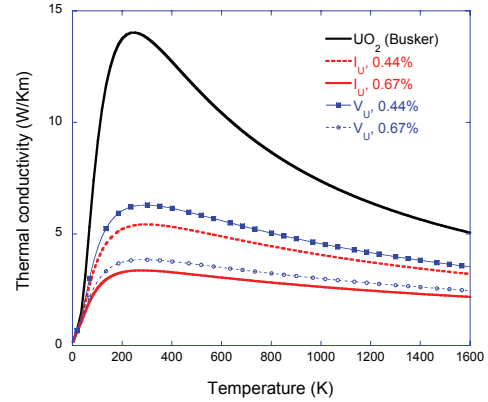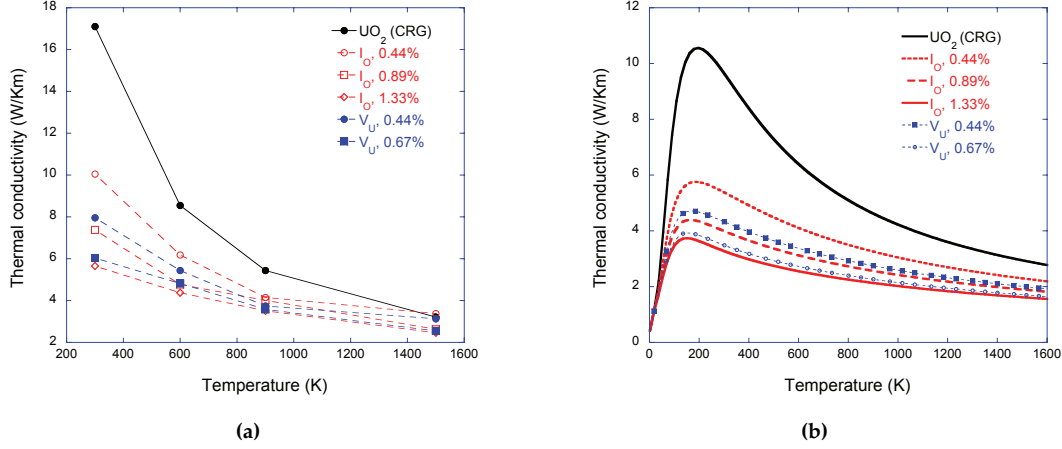
Figure 8: (a) The effect of I_O and V_O defects on the thermal conductivity of UO_2, at different temperatures. (b) Thermal conductivity of UO_2 containing oxygen defects, including correction for spin-phonon scattering. These results were obtained from the data in (a) by adding the spin-phonon scattering contribution derived from experimental data. (c) The effect of I_U and V_U defects on the thermal conductivity of UO_2, at different temperatures. (d) Thermal conductivity of UO_2 containing uranium defects, including correction for spin-phonon scattering. All MD simulations employ the Busker potentials.

most significant for uranium and oxygen defects when accounted for by uranium defects (see Figures 8d and 9b) compared to oxygen defects (see Figures 8b and 9b). For all results the effect of uranium and oxygen defects is highly dependent on temperature, whereby very little degradation of thermal conductivity is predicted for high temperatures where the phonon mean free path is limited by Umklapp processes [82].


Figure 9: (a) The effect of I_O and V_U defects on the thermal conductivity of UO_2, as a function of temperature. All MD simulations employ the CRG potential. (b) The UO_2 thermal conductivity including oxygen and uranium point defects adjusted for spin-phonon scattering.

5.4. The Callaway defect scattering parameter D'

Figure 10a and Table 7 show the D' parameters resulting from fitting to MD data for various fission products and uranium and oxygen defects. For both potentials Pu exhibits the lowest scattering, while Zr has the lowest scattering of the fission products. The La D' parameter is noticeably greater than for Zr using the CRG potential, while a marginal increase is seen using the Busker potential. As discussed previously, although La is more similar in size to U, the effect of charge imbalance that is not present for Zr accounts for the greater scattering due to La. Nonetheless, the D' parameter for Xe is very high in comparison to those for other fission products, Zr and La. This is in line with the results of Tonks *et al.* [4], who also identify the proportion of gas that is in solution compared to that which forms bubbles as a very important parameter for realizing the true impact of Xe on nuclear fuel thermal conductivity. Their results indicate that the degradation in thermal conductivity of real nuclear fuel is largely accounted for by considering just the Xe contribution. As corroborated by our results, this implies that the other fission products are far less significant. In addition, using both potentials the D' values for uranium defects are notably greater than for oxygen vacancies and interstitials. In general, both the CRG and Busker potentials predict similar trends.

5.5. Simple analytical expression of defect scattering

As discussed in the methodology (see section 2) many fuel performance codes use a simple high-temperature analytical expression for thermal conductivity (equation 8), whereby the scattering strength of a given species is defined by C and the temperature dependent behavior of pure UO_2 is governed by A and B. Firstly, A and B are fitted to the spin adjusted pure
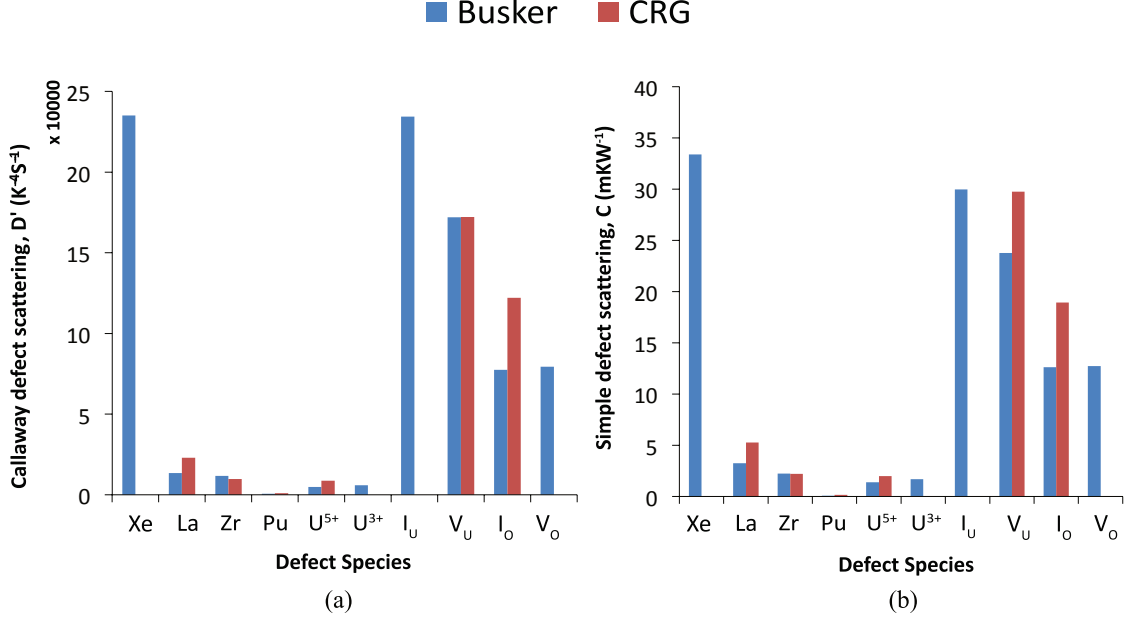
Figure 10: The defect scattering parameters for a) the Callaway model, D', and b) the simple analytical model, C. Parameters are reported for a variety defect species using the Busker potential (blue) the CRG potential (red). All defects are fully charge compensated with U^{5+} or U^{3+} within the simulation. Isolated U^{5+} and U^{3+} results are also given. The parameters are reported in Table 7.

UO$_2$ data above 500 K, shown in Figure 6. For the Busker potential $A = 3.46 \times 10^{-2}$ mKW^{-1} and $B = 1.01 \times 10^{-4}$ mW^{-1}, while for the CRG potential $A = 3.11 \times 10^{-2}$ mKW^{-1} and $B = 2.08 \times 10^{-4}$ mW^{-1}. The difference in A and B between the Busker potential and the CRG potential is due to their disagreement in the description of the pure UO$_2$ lattice, as is clearly seen in Figure 6. Particularly, this is true for B (which describes phonon-phonon interactions), for which there is a factor of two difference between the potentials. Experimental $A = 0.115$ mKW^{-1} and $B = 2.48 \times 10^{-4}$ mW^{-1} values from Wiesenack *et al.* [94] show good agreement with the CRG potential for the B term, while additional temperature independent factors may account for a larger A term. Furthermore, previous work by Cooper *et al.* [26] for the CRG potential without adjustment for spin-scattering reported a similar value for the phonon-phonon scattering B parameter and a lower A parameter, thus confirming that A accounts for the additional spin scattering process.

The resulting C parameters from fitting to spin adjusted MD data above 500 K are reported in Figure 10b and Table 7 showing the same trends as for the Callaway D' parameters. Despite the disagreement between the potentials on the thermal conductivity of pure UO$_2$, there is a reasonable agreement for the defect scattering terms. These simple analytical parameters for defect scattering are readily implemented in a wide variety of fuel performance codes, following the example of Tonks *et al.* [4].

To understand the microscopic origins of the phonon scattering by defects, it is desirable to deconvolute the different terms that contribute to C. In the literature, it is commonly assumed that both the mass difference and the volume difference of defects are primarily responsible for scattering strength, with the latter describing the misfit strain field in the neighborhood of the defect, formulated by Abeles for the phonon scattering cross section [95]. Following preliminary

failures to account for our MD determined C parameters by using such models, we propose that a more complex approach ought to be taken to remedy these differences. Although beyond the scope of this work, one ought to investigate, in addition to mass and volume differences, the effect of bond formation/breakage and deviations in the elastic constants [79] as bound or isolated defects are introduced to the system.

Table 7: Defect scattering parameters, D' for the Callaway model (equation 7) and C for the simple analytical model (equation 8), fitted to MD data with charge compensation by U^{5+} or U^{3+}. These parameters are also reported in Figure 10.

	Analytical, C (mKW^{-1})		Callaway model, D' (K^{-4}S^{-1})	
	Busker	CRG	Busker	CRG
Xe	33.9	-	235000	-
La	3.97	5.28	13500	22900
Zr	2.23	2.20	11800	9720
Pu	0.0777	0.156	563	953
U^{5+}	1.38	1.99	4850	8730
U^{3+}	1.68	-	5890	-
I_U	29.98	-	234000	-
V_U	23.78	32.74	172000	172000
I_O	12.63	18.94	77400	122000
V_O	12.74	-	79400	-

5.6. Charge compensation effect

So far we have only considered uranium and oxygen defects in the context of non-stoichiometry, whereby full charge compensations by U^{5+} and U^{3+} are applicable. However, it is also useful to consider background charge compensated defects in the context of, e.g., radiation damage where Frenkel pair generation maintains charge neutrality. The background charge compensated values for uranium and oxygen defects can be combined with the background charge compensated values for fission products to give an estimate for the degradation of thermal conductivity due to fission products depending on the degree of non-stoichiometry and thus the mechanism for charge compensation (this is demonstrated below for La). Figure 11 reports D' using the CRG potential for oxygen and uranium defects in the case of a) V_O, I_O, V_U and I_U defects only (with a charge neutralising background jellium), b) charge compensation of I_O and V_U by U^{5+} within the simulation cell and c) a combination of I_O, V_U and U^{5+} D' parameters from (a), for example by summing the D' value for I_O with $2D'$ for U^{5+}. Due to the unavailability of U^{3+} with the CRG potential, the results for V_O and I_U are only reported for case (a). The data plotted in Figure 11 are also reported in Table 8 alongside the analytical C, parameters determined by fitting equation 8 to the spin-scattering adjusted MD data above 500 K. It is interesting to note that in the case of background charge compensated defects, oxygen interstitials exhibit greater scattering than uranium vacancies. However, the scattering parameters are increased significantly when accounting for charge compensation either b) within the simulation itself or c) by combining $D'(U^{5+})$ with $D'(V_U)$ or $D'(I_O)$. This effect is most significant for V_U which requires twice as many U^{5+} charge compensating defects as for I_O. Interestingly, when charge compensation of V_U is included within the MD simulation cell there is a particularly drastic effect on D'. There are several possible reasons for this. By randomly distributing such a high concentration of U^{5+} defects within the simulation cell, high energy unfavorable configurations may be formed that create a disproportionate scattering effect. Whether this effect is an accurate representation of real nuclear fuel is unclear. On the other hand, it is also possible that
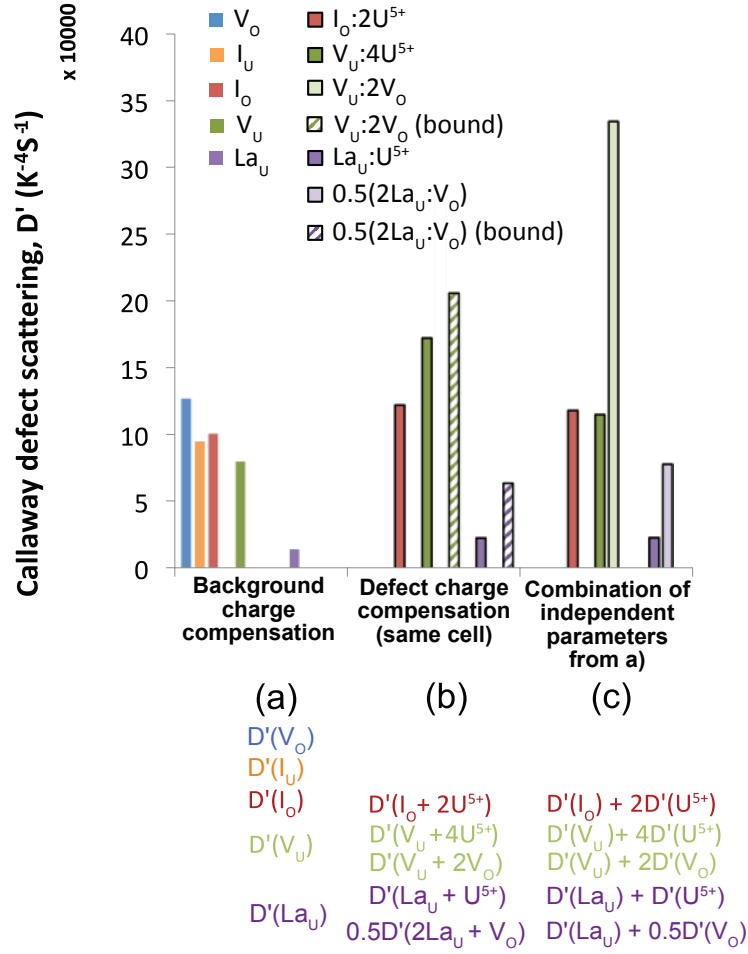
20

this effect is simply because of the difference in the scattering behavior of charge compensated and background charge compensated uranium vacancies due to the Coulombic interactions.

Figure 11 also reports D' using the CRG potential for La in the case of a) La^{3+} defects only, b) charge compensation of La^{3+} by U^{5+} within the simulation cell and c) a combination of La^{3+} and U^{5+} D' parameters from (a), by summing the D' values. The difference between charge compensated in the same box and the combination of individual scattering parameters is negligible for the La case. Furthermore, due to the mixed U^{5+} and V$_O$ charge compensation mechanism for La^{3+} in stoichiometric UO$_2$ [86, 87], we have also considered case by combining D' for La^{3+} with $\frac{1}{2}D'$ for V$_O$. Figure 11c) shows that if La is charge compensated by V$_O$ (solid light purple bar) then it has a greater impact on thermal conductivity than if it is compensated by U^{5+} (solid purple bar). The proportion of La^{3+} charge compensated by a given defect is dependent on the degree of non-stoichiometry in the system. Our results can be combined with models that predict the appropriate proportions of charge compensating defects as a function of non-stoichiometry and temperature to derive the degradation of thermal conductivity.

In the previous discussion, we applied background charge compensated defects to obtain the total combined scattering effect. This is a valid approach to estimate the combined effect of scattering if the defects are randomly distributed and weakly interacting. As a benchmark, by comparing the results from combination of individual defects against results with charge compensating defects in the same cell (randomly distributed defects in the dilute limit), we found excellent agreement for both the 2La$_U$ + V$_O$ and V$_U$ + 2V$_O$ cases within statistical and fitting errors. However, strongly interacting defects must be treated explicitly, since compact clusters of defects, such as the bound 2La$_U$:V$_O$ or V$_U$:2V$_O$ defects, can have different scattering strengths than the combination of the results for individual defects, 2La$_U$ + V$_O$ or V$_U$ + 2V$_O$, which models randomly distributed dilute defects. For the compact clusters, there is roughly only a third of the concentration of scattering centers compared to the randomly distributed defects, in a simplified view of counting one compact cluster as a single scattering center. To gain understanding of the effect of compact cluster defects, we performed additional MD simulations using the CRG potential for the two fully clustered 2La$_U$:V$_O$ and V$_U$:2V$_O$ defects. The results for the scattering parameter D' are reported in Figure 11b) while the summation of the D' values from individual defects is reported in Figure 11c). Comparing the scattering from clusters of defects and combined results from individual defects, the former exhibits reduced total scattering as is expected from the lower concentration of defect scattering centers, with a 15% decrease in the D' value for the 2La$_U$:V$_O$ case, and a 33% decrease in the D' value for the V$_U$:2V$_O$ case, as shown in Figure 11. We note that this is not equivalent to the difference in the concentration of scattering centers, as discussed above. In addition, the level of reduction is also different in the 2La$_U$:V$_O$ than in the V$_U$:2V$_O$ case, thereby suggesting a more complicated mechanism involved than just the concentration of scattering centers.

Table 8: Defect scattering parameters, D' for the Callaway model (equation 7) and C for the simple analytical model (equation 8), fitted to MD data of defects with charge compensation by a uniform background jellium. These parameters are also reported in Figure 11a).

	Analytical, C (mKW^{-1})	Callaway model, D' (K^{-4}S^{-1})
I$_U$	18.91	95000
V$_U$	16.11	80000
I$_O$	17.78	100700
V$_O$	21.38	126800
La	2.37	14500

Figure 11: The defect scattering parameters for the Callaway model, D', is shown for oxygen vacancies and interstitials, cation vacancies and interstitials, and La fission product. Results are shown for a) charge compensation by a uniform background charge, b) charge compensation by U^{5+} species and anion defects in the same simulation cell and c) by combining the separate D' parameters. See the text for details. The parameters are also reported in Table 8.

5.7. Validation against experimental measurements of UO_2 and UO_{2+x} thermal conductivity
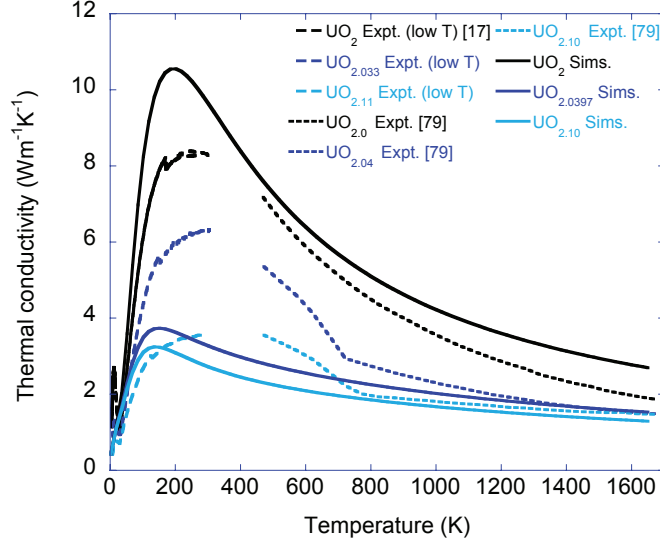
Figure 12: Comparison of the UO_{2+x} thermal conductivity obtained from MD simulations and from experiments. The high temperature experimental data were taken from White and Nelson [79] and the low temperature data are from the present study (UO_{2+x}) or from Gofryk et al. [17] (UO_2). The low temperature experimental data were obtained by measurements on single crystals oriented in the [111] crystallographic direction.

In order to validate the modeling results, comparison is made to experimental measurements on single crystal hyper-stoichiometric UO_{2+x} samples and high-temperature literature data [79]. This establishes the extent of defect scattering by I_O and U^{5+} cations. These samples were prepared from the same bulk UO_2 single crystal as used for the stoichiometric UO_2 measurements in Ref. [17]. The defect concentrations in UO_{2+x} can be accurately determined by careful control of the oxygen stoichiometry [96]. The oxygen-to-metal (O/M) ratio of the urania single crystals was set in a thermogravimetric analyzer (STA 409PG, Netzsch Instruments) by controlling the oxygen activity. O/M was initially set to 2.00 and then subsequently adjusted to the hyper-stoichiometric values by adjusting the partial pressure of oxygen at 1000°C. Final stoichiometry was calculated from the sample weight change relative to the stoichiometric $UO_{2.00}$ reference state. The measurements were performed with a Physical Property Measurement System-9 from Quantum Design (continuous mode, 0.1 Kmin^{-1}) from 4 K to 300 K. Comparison is also made with higher temperature literature data for further validation and to avoid complications of UO_2-U_4O_9 phase transitions occurring at low temperatures [97].

The MD simulations for UO_{2+x} (corrected for resonant spin–phonon scattering) employing the CRG potential are compared to experimental measurements in Figure 12. White and Nelson [79] reported the thermal conductivity for a range of UO_{2+x} stoichiometries at high temperature. Above ~800 K the MD simulations are in good agreement with the measured thermal conductivity, while it is substantially underestimated below this temperature. The change in thermal conductivity with increasing oxygen content is correctly reproduced in each temperature range. One complication in comparing the MD and experimental results is the strong tendency of UO_{2+x} to phase separate into UO_2+U_4O_9. The transition to a single UO_{2+x} phase

occurs at $\sim$800 K and it is responsible for the kink in the experimental thermal conductivity measurements [12, 79]. The mixed $UO_2+U_4O_9$ phase has much higher thermal conductivity than the corresponding disordered UO_{2+x} phase, which is understood in terms of the increased point defect scattering in UO_{2+x} compared to UO_2. The MD simulations model perfectly disordered UO_{2+x}, which is only relevant well above 800 K. The $UO_2+U_4O_9$ phase separation explains why the MD thermal conductivity is lower than the experimental results below 800 K.

5.8. Modeling U_4O_9

To remedy the difference between experiment and modeling for low temperature UO_{2+x} caused by phase separation to $UO_2+U_4O_9$, we investigated the thermal conductivity of U_4O_9 by MD using the CRG potential. The structure of Andersson *et al.* [73] (Figure 4) was used so that U^{4+} and U^{5+} positions could be assigned based on DFT calculations. The same MD method as for UO_2 was applied to U_4O_9. Figure 13 shows that MD predictions exceeded the thermal conductivity measurements of White and Nelson [79]. Therefore the $A = 3.11 \times 10^{-2}$ mKW^{-1} parameter from equation 8, which represents spin scattering, was used with equation 11 to modify the U_4O_9 MD data:

$$\kappa_s = (A + \frac{1}{\kappa_{ns}})^{-1} \qquad (11)$$

where κ_s is the spin scattering adjusted data (red triangles, Figure 13) and κ_{ns} is not adjusted for spin scatering (blue diamonds, Figure 13). It is clear that by adjusting for spin scattering the
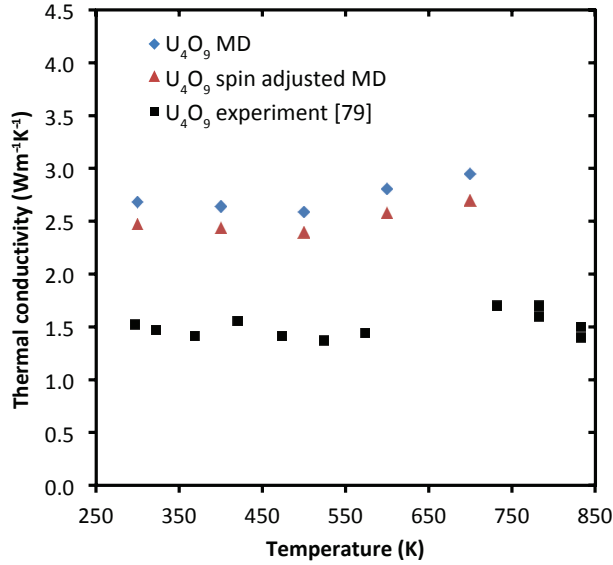
Figure 13: The thermal conductivity of U_4O_9 as a function of temperature predicted by MD simulations using the CRG potential (blue diamonds), MD simulations adjusted for magnetic scattering (red triangles) and the experimental measurements of White and Nelson [79].

thermal conductivity of U_4O_9 is not sufficiently reduced to mitigate the discrepancies between modeling and experiment. To test if this is due to inaccuracies in the DFT predicted crystal structure, the experimental structure of Masaki and Doi *et al.* [98] was also tested. The same result was obtained as for the DFT structure, indicating that the difference between experiment and modelling is due to the interatomic potential used. Work is also being undertaken to couple

24

the predictions of the thermal conductivity of UO_{2+x} and U_4O_9 with microstructural modeling of the low temperature phase separation discussed in section 5.7.

5.9. Modeling thermal conductivity using the Green-Kubo method

The Green-Kubo (GK) method [99, 100] is an equilibrium MD technique to compute thermal conductivity. In the GK method, using the fluctuation-dissipation theorem from linear response theory, the thermal conductivity κ is computed from

$$\kappa = \frac{1}{3k_B V T^2} \int_0^\infty \langle \mathbf{J}(t) \cdot \mathbf{J}(0) \rangle dt \tag{12}$$

where V is the volume of the system, $\mathbf{J}$ is the heat current vector, t is time, and $\langle \mathbf{J}(t) \cdot \mathbf{J}(0) \rangle$ is the heat current auto correlation function (HCACF). The thermal heat current is,

$$\mathbf{J}(t) = \sum_i \mathbf{v}_i E_i + 1/2 \sum_{i \neq j} \mathbf{r}_{ij}(\mathbf{F}_{ij} \cdot \mathbf{v}_i) \tag{13}$$

where $\mathbf{v}_i$ and E_i are the velocity vector and the energy of atom i in the system, $\mathbf{r}_{ij} = \mathbf{r}_i - \mathbf{r}_j$ and $\mathbf{F}_{ij}$ is the force acted on atom i due to its neighbor j form the interatomic potential. The GK method offers an alternative method to compute the thermal conductivity through MD simulations [101–104]. Additionally, since the GK method is an equilibrium MD technique in a homogeneous equilibrium system, in which no directional driving force is imposed, the GK method offers a possibly excellent benchmark for assessing the statistical variations for thermal transport in UO_2 containg defects and fission products. This is currently an ongoing work and here we only report some early phase of the study.

In MD simulations, since the simulation is performed for discrete MD timestep of Δt, the previous equation becomes,

$$\kappa_{ij}(\tau) = \frac{\Delta t}{k_B V T^2} \sum_{m=1}^{M} (N-m)^{-1} \sum_{n=1}^{N-m} J_i(m+n) J_j(n) \tag{14}$$

where the correlation time τ is equal to $M\Delta t$, $J_i(m)$ is the ith component of the heat current at MD timestep m, N is the total MD simulation steps. The final thermal conductivity κ is, $(\kappa_{11} + \kappa_{22} + \kappa_{33})/3$. In the GK method, both the total MD simulation steps N and the correlation time τ are important parameters to explore that can influnce the thermal conductivity results. The correlation time τ, which defines the number of integration steps in the HCACF, is especially important, and has to be treated with care.

Using the GK method, MD simulations of the thermal conductivity of UO_2 at 1500 K was carried out. A periodic supercell containing $6 \times 6 \times 6$ unit cells of fluorite UO_2 was constructed. The system was equilibrated in NPT ensemble at 1500 K for 50 ps, then switched to NVE ensemble for 1 ns during which HCACF funtion values were evaluated. The correlation time τ was chosen to be 1 ps. The Figure 14a shows the thermal conductivity of UO_2 at 1500 K obtained through the GK method as a function of the MD simulation time. It can seen that the simulation time is long enough to obtain converged thermal conductivity result. In Figure 14b, the corresponding scaled HCACF function (with the scaling factor same as the prefactor in Eq. 12) as a function of correlation time is shown. Due to the optical phonon between U ions and O ions, the HCACF values have strong oscillations but decaying to zero as the correlation time increases. At 1 ps, the correlations are well captured. This is also supported by Figure 14c, where the integrated HCACF, or thermal conductivity, is shown to be nearly converged as a function of the correlation time. Currently, work is being undertaken to extend such study to UO_2 at different temperatures and UO_2 containing defects.

(a)

(b)

(c)
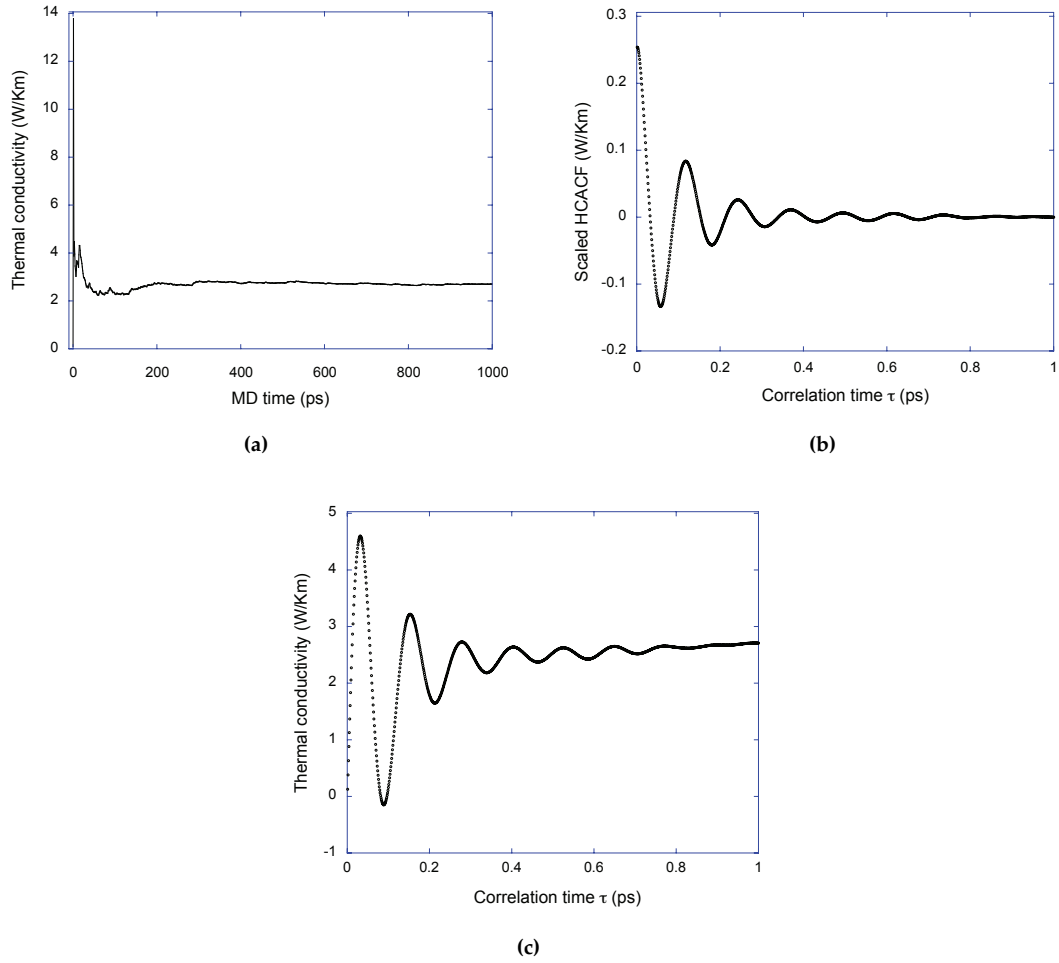
Figure 14: (a) Using the Green-Kubo method, the thermal conductivity at 1500 K as a function of MD simulation time. (b) The corresponding scaled HCACF function as a function of correlation time for MD simulation time of 1 ns. (c) The thermal conductivity as a function of correlation time for MD simulation time of 1 ns.

6. Conclusions

Thermal transport in UO_2 with uranium and oxygen defects and fission products has been investigated using non-equilibrium MD simulations. Two sets of empirical potentials are used to study the degradation of UO_2 thermal conductivity. One is based on the standard Buckingham type interatomic potential and the other on a recently developed potential that combines the many-body EAM potential with Morse-Buckingham pair potentials. New parameter sets for the U^{5+} and Zr^{4+} are developed for the many-body potential. Although we only use the Zr^{4+} potential for the simulation of Zr in UO_2, it has also been successfully validated for the tetragonal ZrO_2 system. The thermal conductivity results from the MD simulations are then fitted to the Callaway model. In order to improve the accuracy of the thermal conductivity predictions, these results are corrected for the spin-phonon scattering mechanism by adding the corresponding relaxation time derived from existing experimental data. Very high defect scattering is predicted for Xe compared to those of La and Zr. Uranium defects reduce the thermal conductivity more than oxygen defects. For each defect and fission product, scattering parameters are derived for application in both a Callaway model and the corresponding high-temperature model typically used in nuclear fuel performance codes. The effect of charge compensation for uranium and oxygen defects was also examined indicating that background charge compensated uranium vacancies scatters less than oxygen interstitials. However, the reverse was true when considering full charge compensation as this requires $4U^{5+}$ for uranium vacancies compared to just $2U^{5+}$ for oxygen interstitials. Finally, to validate the modeling results, comparisons were made with experimental measurements on single crystal hyper-stoichiometric UO_{2+x} samples and literature values. At high temperatures above ~ 800 K the MD simulations are in good agreement with the measured thermal conductivity, while it is substantially underestimated below this temperature, which is due to the mixed UO_2 and U_4O_9 phases. The change in thermal conductivity with increasing oxygen content is correctly reproduced in each temperature range.

In this work we have presented a modeling approach to de-convolute the effect of different fission products, transmutation products and uranium and oxygen defects on the thermal conductivity of UO_2. Fuel performance codes [1–3], used extensively in the industry to underpin reactor operation and safety, can combine these parameters with models that predict radiation damage and fission product distribution [4] throughout the fuel. The comprehensive and consistent parameters derived here are readily applied in fuel performance codes to enhance their predictive capabilities and form part of greater body of work to improve thermal conductivity models for fuel [6].

Two aspects of ongoing works are briefly reported. One aspect is focused on investigating the effect of phase separation to $UO_2+U_4O_9$ on the low temperature thermal conductivity of UO_{2+x}. MD calculations of U_4O_9 thermal conductivity will be coupled to mesoscale modeling of microstructure in order to remedy difference between modeling experimental results. Another ongoing work is focused on exploration of computation of thermal conductivity using the Green-Kubo method. Since the Green-Kubo method is an equilibrium MD technique in a homogeneous equilibrium system, in which no directional driving force is imposed, it offers a possibly excellent benchmark for assessing the statistical variations for thermal transport in UO_2 containing defects and fission products.

[1] P. A. Jackson, J. A. Turnbull, R. J. White, A Description of the ENIGMA Fuel Performance Code, Technical Report IAEA-TECDOC-687, International Atomic Energy Agency, 1989.

[2] P. A. Jackson, J. A. Turnbull, R. J. White, Nuclear energy 29 (1990) 107–114.

[3] R. L. Williamson, J. D. Hales, S. R. Novascone, M. R. Tonks, D. Gaston, C. J. Permann, D. Andrs, R. C. Martineau, J. Nucl. Mater. 423 (2012) 149–163.

[4] M. R. Tonks, X.-Y. Liu, D. A. Andersson, D. Perez, A. Chernatynskiy, G. Pastore, C. R. Stanek, R. Williamson, J. Nucl. Mater. 469 (2016) 89–98.

[5] C. Unal, B. Williams, A. Yacout, D. Higdon, Nucl. Eng. Design 263 (2013) 102–128.

[6] An Empirical Model of UO_2 Thermal Conductivity Based of Laser Flash Measurements of Thermal Diffusivity, Technical Results TR-111347, Electric Power Research Institute, 1998.

[7] W. Lyon, R. Montgomery, S. Yagnik, Proc. 2004 Int. Meeting on LWR Fuel Performance (2004) 1090.

[8] High Burn-Up Properties of the Fuel Variants Irradiated in IFA-649, Technical Results TR-1025200, Electric Power Research Institute, 2013.

[9] Thermophysical Properties Database of Matertials for Light Water Reators and Heavy Water Reactors, Technical Report IAEA-TECDOC-1496, International Atomic Energy Agency, 2006.

[10] C. Ronchi, M. Sheindlin, M. Musella, G. J. Hyland, J. App. Phys. 85 (1999) 776.

[11] C. Ronchi, M. Sheindlin, D. Staicu, M. Kinoshita, J. Nucl. Mater. 327 (2004) 58–76.

[12] M. Amaya, T. Kubo, Y. Korei, J. Nucl. Sci. Tech. 33 (1996) 636–640.

[13] M. Amaya, M. Hirai, H. Sakurai, K. Ito, M. Sasaki, T. Nomata, K. Kamimura, R. Iwasaki, J. Nucl. Mater. 300 (2002) 57–64.

[14] T. Watanabe, S. B. Sinnott, J. S. Tulenko, R. W. Grimes, P. K. Schelling, S. R. Phillpot, J. Nucl. Mater. 375 (2008) 388–396.

[15] T. Uchida, T. Sunaoshi, M. Kato, K. Konashi, Prog. Nucl. Sci. Tech. 2 (2011) 598–602.

[16] A. Chernatynskiy, C. Flint, S. Sinnott, S. R. Phillpot, J. Mater. Sci. 47 (2012) 7693–7702.

[17] K. Gofryk, S. Du, C. R. Stanek, J. C. Lashley, X.-Y. Liu, R. K. Schulze, J. L. Smith, D. J. Safarik, D. D. Byler, K. J. McClellan, B. P. Uberuaga, B. L. Scott, D. A. Andersson, Nat. Commun. 5 (2014) 4551.

[18] J. W. L. Pang, W. J. L. Buyers, A. Chernatynskiy, M. D. Lumsden, B. C. Larson, S. R. Phillpot, Phys. Rev. Lett. 110 (2013) 157401.

[19] Q. Yin, S. Y. Savrasov, Phys. Rev. Lett. 100 (2008) 225504.

[20] S. Yamasaki, T. Arima, K. Idemitsu, Y. Inagaki, Int. J. Thermophys. 28 (2007) 661–673.

[21] T. Watanabe, S. G. Srivilliputhur, P. K. Schelling, J. S. Tulenko, S. B. Sinnott, S. R. Phillpot, J. Am. Ceram. Soc. 92 (2009) 850–856.

[22] S. Nichenko, D. Staicu, J. Nucl. Mater. 433 (2013) 297–304.

[23] M. R. Tonks, P. C. Millett, P. Nerikar, S. Du, D. A. Andersson, C. R. Stanek, D. Gaston, D. Andrs, R. Williamson, J. Nucl. Mater. 440 (2013) 193–200.

[24] B. Deng, A. Chernatynskiy, P. Shukla, R. E. Stoller, S. B. Sinnott, S. R. Phillpot, J. Nucl. Mater. 434 (2013) 203–209.

[25] C.-W. Lee, A. Chernatynskiy, P. Shukla, R. E. Stoller, S. B. Sinnott, S. R. Phillpot, J. Nucl. Mater. 456 (2015) 253–259.

[26] M. W. D. Cooper, S. C. Middleburgh, R. W. Grimes, J. Nucl. Mater. 466 (2015) 29–35.

[27] T. Arima, S. Yamasaki, Y. Inagaki, K. Idemitsu, J. Alloys Compd. 415 (2006) 43–50.

[28] J.-J. Ma, J. Zheng, M.-J. Wan, J.-G. Du, J. Yang, G. Jiang, J. Nucl. Mater. 452 (2014) 230–234.

[29] Neelmani, G. S. Verma, Phys. Rev. B 6 (1972) 3509–3515.

[30] J. Moore, D. McElroy, J. Am. Ceram. Soc. 54 (1971) 40–46.

[31] R. Caciuffo, G. Amoretti, P. Santini, G. H. Lander, J. Kulda, P. de V. Du Plessis, Phys. Rev. B 59 (1999) 13892.

[32] R. Caciuffo, P. Santini, S. Carretta, G. Amoretti, A. Hiess, N. Magnani, L.-P. Regnault, G. H. Lander, Phys. Rev. B 84 (2011) 104409.

[33] S. L. Dudarev, P. M. Derlet, J. Phys.: Condens. Matter 17 (2005) 7097–7118.

[34] G. Busker, A. Chroneos, R. W. Grimes, I. W. Chen, J. Am. Ceram. Soc. 82 (1999) 1553–1559.

[35] M. W. D. Cooper, M. J. D. Rushton, R. W. Grimes, J. Phys. Condens. Matter. 26 (2014) 105401.

[36] P. Jund, R. Jullien, Phys. Rev. B 59 (1999) 13707–13711.

[37] F. MullerPlathe, J. Chem. Phys. 106 (1997) 6082–6085.

[38] T. Ikeshoji, B. Hafskjold, Mol. Phys. 81 (1994) 251–261.

[39] X. Zhou, S. Aubry, R. E. Jones, A. Greenstein, P. K. Schelling, Phys. Rev. B 79 (2009) 115201.

[40] S. Plimpton, J. Comp. Phys 117 (1995) 1–19.

[41] P. C. Howell, J. Comput. Theor. Nanos. 8 (2011) 2129–2143.

[42] R. A. Buckingham, Proc. Roy. Soc. Lond. Ser. A Math. Phys. Sci. 168 (1938) 264–283.

[43] P. M. Morse, Phys. Rev. B 34 (1929) 57–64.

[44] M. S. Daw, M. I. Baskes, Phys. Rev. B 29 (1984) 6443–6453.

[45] R. W. Grimes, C. R. A. Catlow, Phil. Trans. R. Soc. Lond. A 335 (1991) 609–634.

[46] R. G. J. Ball, R. W. Grimes, J. Chem. Soc., Faraday Trans. 86 (1990) 1257–1261.

[47] L. Minervini, Atomistic Simulations of Defective Oxides, Ph.D. thesis, Imperial College (2000).

[48] A. Cleave, Atomic Scale Simulations for Waste Form Applications, Ph.D. thesis, Imperial College (2000).

[49] B. E. Hanken, C. R. Stanek, N. Grønbech-Jensen, M. Asta, Phys. Rev. B 84 (2011) 085131. doi:10.1103/PhysRevB.84.085131.

[50] M. J. D. Rushton, A. Chroneos, Sci. Rep. 4 (2014) 6068.

[51] M. W. D. Cooper, S. T. Muprhy, , M. J. D. Rushton, R. W. Grimes, J. Nucl. Mater. 461 (2015) 206–214.

[52] D. Wolf, P. Keblinski, S. R. Phillpot, J. Eggebrecht, J. Chem. Phys. 110 (1999) 8254–8282.

[53] J. Callaway, Phys. Rev. 113 (1959) 1046–1051.

[54] G. Dolling, R. Cowley, A. Woods, Can. J. Phys. 43 (1965) 1397.

[55] P. K. Schelling, S. R. Phillpot, D. Wolf, J. Am. Ceram. Soc. 84 (2001) 1609–1619.

[56] B. Bondars, G. Heidemane, J. Grabis, K. Laschke, H. Boysen, J. Schneider, F. Frey, J. Mater. Sci. 30 (1995) 1621.

[57] P. Aldebert, J.-P. Traverse, J. Am. Ceram. Soc. 68 (1985) 34.

[58] G. Teufer, Acta Cryst. 15 (1962) 1187.

[59] J. D. Gale, J. Chem. Soc. 93 (1997) 629.

[60] J. P. Perdew, K. Burke, M. Ernzerhof, Phys. Rev. Lett. 77 (1996) 3865–3868.

[61] H. J. Monkhorst, J. D. Pack, Phys. Rev. B 13 (1976) 5188–5192.

[62] A. Walker, D. Wilson, github.com/andreww/elastic-constants (downloaded 2015).

[63] M. W. D. Cooper, S. T. Murphy, P. C. M. Fossati, M. J. D. Rushton, R. W. Grimes, Proc. Roy. Soc. Lond. A 470 (2014) 20140427.

[64] R. D. Shannon, Acta Crystallogr. A (1976) 751.

[65] E. H. Kisi, C. J. Howard, J. Am. Ceram. Soc. 84 (1998) 1682.

[66] G. Fadda, L. Colombo, G. Zanzotto, Phys. Rev. B 79 (2009) 214102.

[67] Y. Natanzon, M. Boniecki, Z. Lodziana, J. Phys. Chem. Solids 70 (2009) 15–19.

[68] J. E. Lowther, Phys. Rev. B 73 (2006) 134110.

[69] V. Milman, A. Perlov, K. Refson, S. J. Clark, J. Gavartin, D. Winkler, J. Phys. Condens. Matter 21 (2009) 485404.

[70] P. Bouvier, E. Djurado, G. Lucazeau, T. Le Bihan, Phys. Rev. B 62 (2000) 8731.

[71] C. J. Howard, R. J. Hill, B. E. Reichert, Struct. Sci 44 (1988) 116.

[72] H. G. Scott, J. Mater. Sci. 10 (1975) 1527.

[73] D. A. Andersson, G. Baldinozzi, L. Desgranges, D. R. Conradson, S. D. Conradson, Inorg. Chem. 52 (2013) 2769–2778.

[74] G. C. Allen, N. R. Holmes, J. Nucl. Mater. 223 (1995) 231.

[75] L. Lynds, W. A. Young, J. S. Mohl, G. G. Libowitz, Am. Chem. Soc. Adv. Chem. Ser. 39 (1963) 58.

[76] R. E. Rundle, N. C. Baenziger, A. S. Wilson, R. A. McDonald, J. Amer. Chem. Soc. 70 (1948) 99.

[77] P. Perio, Bull. Soc. Chim (1953) 256.

[78] F. Grønvold, J. Inorg. Nucl. Chem. 1 (1955) 357–370.

[79] T. White, A. T. Nelson, J. Nucl. Mater. 443 (2013) 342.

[80] K. Govers, S. Lemehov, M. Hou, M. Verwerft, J. Nucl. Mater. 376 (2008) 66–77.

[81] S. I. Potashnikov, A. S. Boyarchenkov, K. A. Nekrasov, A. Y. Kupryazhkin, J. Nucl. Mater. 419 (2011) 217–225.

[82] R. Peierls, Ann Physik 5 (1932) 121.

[83] X.-Y. Liu, D. A. Andersson, B. P. Uberuaga, J. Mater. Sci. 47 (2012) 7367–7384.

[84] X.-Y. Liu, D. Andersson, J. Nucl. Mater. 462 (2015) 8–14.

[85] D. Shin, T. M. Besmann, J. Nucl. Mater. 433 (2013) 227–232.

[86] S. C. Middleburgh, R. W. Grimes, K. H. Desai, P. R. Blair, L. Hallstadius, K. Blackman, P. V. Uffelen, J. Nucl. Mater. 427 (2012) 359–363.

[87] X.-Y. Liu, K. E. Sickafus, J. Nucl. Mater. 414 (2011) 217.

[88] D. A. Andersson, P. Garcia, X.-Y. Liu, G. Pastore, M. Tonks, P. Millett, B. Dorado, D. R. Gaston, D. Andrs, R. L. Williamson, R. C. Martineau, B. P. Uberuaga, C. R. Stanek, J. Nucl. Mater. 451 (2014) 225–242.

[89] R. Perriot, X.-Y. Liu, C. R. Stanek, D. A. Andersson, J. Nucl. Mater. 459 (2015) 90–96.

[90] H. Kleykamp, J. Nucl. Mater. 131 (1985) 221–246.

[91] M. W. D. Cooper, S. C. Middleburgh, R. W. Grimes, J. Nucl. Mat. 438 (2013) 238–245.

[92] S. C. Middleburgh, D. M. King, G. R. Lumpkin, Roy. Soc. Open Sci. 2 (2015) 140292.

[93] R. J. Konings, T. Wiss, O. Beneš, Nat. Mater. 14 (2015) 247.

[94] W. Wiesenack, IAEA Tech. Comm. Meeting on Fission Gas Release and Fuel Rod Chemistry Related to Extended Burnup, IAEA-TECDOC-697, 27 April-1 May 1992, Pembroke, Canada (April 1993).

[95] B. Abeles, Phys. Rev. 131 (1963) 1906–1911.

[96] C. Guéneau, M. Baichi, D. Labroche, C. Chatillon, B. Sundman, J. Nucl. Mater. 304 (2002) 161.

[97] K. Naito, N. Kamegashira, Advances in Nuclear Science and Technology 9 (1976) 99–180.

[98] N. Masaki, K. Doi, Acta Cryst. 28 (1972) 785–791.

[99] M. S. Green, J. Chem. Phys. 22 (1954) 398.

[100] R. Kubo, Rep. Prog. Phys. 29 (1986) 255.

[101] P. J. D. Lindan, M. J. Gillan, J. Phys.: Condens. Matter 3 (1991) 3929.

[102] J. Li, L. Porter, S. Yip, J. Nucl. Mater. 255 (1998) 139–152.

[103] P. K. Schelling, S. R. Phillpot, P. Keblinski, Phys. Rev. B 65 (2002) 144306.

[104] A. J. H. McGaughey, M. Kaviany, Int. J. Heat and Mass Transfer 47 (2004) 1799.